



GROWTH on S190814bv: Deep Synoptic Limits on the Optical/Near-infrared Counterpart to a Neutron Star–Black Hole Merger

Igor Andreoni¹ , Daniel A. Goldstein^{1,35} , Mansi M. Kasliwal¹ , Peter E. Nugent^{2,3} , Rongpu Zhou² , Jeffrey A. Newman⁴ , Mattia Bulla^{5,6} , Francois Foucart⁷, Kenta Hotokezaka⁸ , Ehud Nakar⁹, Samaya Nissanke^{10,11} , Geert Raaijmakers^{10,11} , Joshua S. Bloom^{2,3}, Kishalay De¹, Jacob E. Jencson^{1,12} , Charlotte Ward¹³, Tomás Ahumada¹³ , Shreya Anand¹, David A. H. Buckley¹⁴, Maria D. Caballero-García¹⁵, Alberto J. Castro-Tirado^{16,17}, Christopher M. Copperwheat¹⁸ , Michael W. Coughlin¹ , S. Bradley Cenko^{19,20} , Mariusz Gromadzki²¹, Youdong Hu^{16,22}, Viraj R. Karambelkar¹, Daniel A. Perley¹⁸ , Yashvi Sharma¹, Azamat F. Valeev²³, David O. Cook²⁴ , U. Christoffer Fremdling¹, Harsh Kumar²⁵, Kirsty Taggart¹⁸, Ashot Bagdasaryan¹, Jeff Cooke^{26,27} , Aishwarya Dahiwalé¹, Suhail Dhawan⁶ , Dougal Dobie^{28,29} , Pradip Gatkine¹³ , V. Zach Golkhou^{30,31,36} , Ariel Goobar⁶ , Andreas Guerra Chaves¹⁰ , Matthew Hankins¹ , David L. Kaplan³² , Albert K. H. Kong³³ , Erik C. Kool³⁴ , Siddharth Mohite^{32,37}, Jesper Sollerman³⁴ , Anastasios Tzanidakis¹ , Sara Webb^{26,27} , and Keming Zhang^{3,37}

¹ California Institute of Technology, 1200 East California Blvd., MC 249-17, Pasadena, CA 91125, USA; andreoni@caltech.edu

² Lawrence Berkeley National Laboratory, 1 Cyclotron Road, Berkeley, CA 94720, USA

³ Department of Astronomy, University of California, Berkeley, CA 94720-3411, USA

⁴ Department of Physics and Astronomy and PITT PACC, University of Pittsburgh, PA 15260, USA

⁵ Nordita, KTH Royal Institute of Technology and Stockholm University, Roslagstullsbacken 23, SE-106 91 Stockholm, Sweden

⁶ The Oskar Klein Centre, Department of Physics, Stockholm University, AlbaNova, SE-106 91 Stockholm, Sweden

⁷ Department of Physics, University of New Hampshire, 9 Library Way, Durham NH 03824, USA

⁸ Department of Astrophysical Sciences, Princeton University, Peyton Hall, Princeton, NJ 08544, USA

⁹ Department of Astrophysics, Sackler School of Physics and Astronomy, Tel Aviv University, Tel Aviv 69978, Israel

¹⁰ GRAPPA, Anton Pannekoek Institute for Astronomy and Institute of High-Energy Physics, University of Amsterdam, Science Park 904, 1098 XH Amsterdam, The Netherlands

¹¹ Nikhef, Science Park 105, 1098 XG Amsterdam, The Netherlands

¹² University of Arizona, Steward Observatory, 933 N. Cherry Avenue, Tucson, AZ 85721, USA

¹³ Department of Astronomy, University of Maryland, College Park, MD 20742, USA

¹⁴ South African Astronomical Observatory, P.O. Box 9, Observatory 7935, Cape Town, South Africa

¹⁵ Astronomical Institute, Academy of Sciences of the Czech Republic, Boční II 1401, CZ-141 00 Prague, Czech Republic

¹⁶ Instituto de Astrofísica de Andalucía (IAA-CSIC), Glorieta de la Astronomía s/n, E-18008, Granada, Spain

¹⁷ Departamento de Ingeniería de Sistemas y Automática, Escuela de Ingenieros Industriales, Universidad de Málaga, Unidad Asociada al CSIC, C. Dr. Ortiz Ramos sn, E-29071 Málaga, Spain

¹⁸ Astrophysics Research Institute, Liverpool John Moores University, IC2, Liverpool Science Park, 146 Brownlow Hill, Liverpool L3 5RF, UK

¹⁹ Astrophysics Science Division, NASA Goddard Space Flight Center, MC 661, Greenbelt, MD 20771, USA

²⁰ Joint Space-Science Institute, University of Maryland, College Park, MD 20742, USA

²¹ Astronomical Observatory, University of Warsaw, Al. Ujazdowskie 4, 00-478 Warszawa, Poland

²² Universidad de Granada, Facultad de Ciencias Campus Fuentenueva S/N CP E-18071 Granada, Spain

²³ Special Astrophysical Observatory, Russian Academy of Sciences, Nizhni Arkhyz, 369167, Russia

²⁴ IPAC, California Institute of Technology, 1200 E. California Blvd., Pasadena, CA 91125, USA

²⁵ Indian Institute of Technology Bombay, Powai, Mumbai 400076, India

²⁶ Australian Research Council Centre of Excellence for Gravitational Wave Discovery (OzGrav), Swinburne University of Technology, Hawthorn, VIC, 3122, Australia

²⁷ Centre for Astrophysics and Supercomputing, Swinburne University of Technology, Hawthorn, VIC, 3122, Australia

²⁸ Sydney Institute for Astronomy, School of Physics, University of Sydney, NSW 2006, Australia

²⁹ CSIRO Astronomy and Space Science, P.O. Box 76, Epping, New South Wales 1710, Australia

³⁰ DIRAC Institute, Department of Astronomy, University of Washington, 3910 15th Avenue NE, Seattle, WA 98195, USA

³¹ The eScience Institute, University of Washington, Seattle, WA 98195, USA

³² Center for Gravitation, Cosmology and Astrophysics, Department of Physics, University of Wisconsin–Milwaukee, P.O. Box 413, Milwaukee, WI 53201, USA

³³ Institute of Astronomy, National Tsing Hua University, Hsinchu 30013, Taiwan

³⁴ The Oskar Klein Centre & Department of Astronomy, Stockholm University, AlbaNova, SE-106 91 Stockholm, Sweden

Received 2019 October 29; revised 2019 December 20; accepted 2019 December 30; published 2020 February 20

Abstract

On 2019 August 14, the Advanced LIGO and Virgo interferometers detected the high-significance gravitational wave (GW) signal S190814bv. The GW data indicated that the event resulted from a neutron star–black hole (NSBH) merger, or potentially a low-mass binary BH merger. Due to the low false-alarm rate and the precise localization (23 deg² at 90%), S190814bv presented the community with the best opportunity yet to directly observe an optical/near-infrared counterpart to an NSBH merger. To search for potential counterparts, the GROWTH Collaboration performed real-time image subtraction on six nights of public Dark Energy Camera images acquired in the 3 weeks following the merger, covering >98% of the localization probability. Using a worldwide network of follow-up facilities, we systematically undertook spectroscopy and imaging of optical counterpart candidates. Combining these data with a photometric redshift catalog, we ruled out each candidate as the counterpart to S190814bv and placed deep, uniform limits on

³⁵ Hubble Fellow.

³⁶ Moore-Sloan, WRF Innovation in Data Science, and DIRAC Fellow.

³⁷ LSSTC Data Science Fellow.

the optical emission associated with S190814bv. For the nearest consistent GW distance, radiative transfer simulations of NSBH mergers constrain the ejecta mass of S190814bv to be $M_{\text{ej}} < 0.04 M_{\odot}$ at polar viewing angles, or $M_{\text{ej}} < 0.03 M_{\odot}$ if the opacity is $\kappa < 2 \text{ cm}^2 \text{ g}^{-1}$. Assuming a tidal deformability for the NS at the high end of the range compatible with GW170817 results, our limits would constrain the BH spin component aligned with the orbital momentum to be $\chi < 0.7$ for mass ratios $Q < 6$, with weaker constraints for more compact NSs.

Unified Astronomy Thesaurus concepts: [Neutron stars \(1108\)](#); [Binary stars \(154\)](#); [Gravitational wave sources \(677\)](#); [Gravitational waves \(678\)](#); [Transient sources \(1851\)](#); [Black hole physics \(159\)](#); [Observational astronomy \(1145\)](#)

Supporting material: data behind figure

1. Introduction

Mergers of binaries containing neutron stars and stellar-mass black holes (NSBH mergers) have long been theorized as potential sites of r -process nucleosynthesis (Lattimer & Schramm 1974), which should be detectable by networks of laser interferometers as gravitational-wave (GW) sources (Abadie et al. 2010), potentially harboring optical counterparts (Metzger & Berger 2012) that could be used to help constrain the equation of state (EOS) of dense nuclear matter (Geesaman 2015; Coughlin et al. 2019c), measure the Hubble constant H_0 (Schutz 1986), and probe radiation hydrodynamics in asymmetric conditions and the limits of nuclear stability (Fernández & Metzger 2016). On 2019 August 14, the LIGO and Virgo interferometers detected S190814bv, the first high-confidence GW signal associated with an NSBH merger (The LIGO Scientific Collaboration & the Virgo Collaboration 2019b, 2019d), confirming that NSBH mergers exist and that they produce GWs.

Electromagnetic (EM) emission from NSBH mergers, which is critical to achieve many of the science goals described in the previous paragraph, is currently the subject of considerable theoretical uncertainty (e.g., Mingarelli et al. 2015; Barbieri et al. 2019; Hotokezaka & Nakar 2019). At this time, it is not clear whether optical/near-infrared (NIR) counterparts to NSBH mergers exist and, if they do, what their properties might be. The uncertainty in the nature of EM counterparts to NSBH mergers is driven primarily by (1) uncertainties in the optical opacity of r -process elements in low ionization states, which may be the dominant opacity affecting spectrum synthesis in NSBH optical counterparts (“kilonovae,” or “macronovae”); (2) a lack of knowledge regarding the EOS of dense nuclear matter, which directly affects the distribution of the merger ejecta and the post-merger nucleosynthesis; (3) an incomplete theoretical picture of the properties of NSBH matter outflows for all potential progenitor configurations; and (4) the complexity of the multiphysics simulations required to predict the observable properties of NSBH mergers, which at various stages must include sophisticated treatments of magnetohydrodynamics, general relativity, neutrino transport, radiation transport, and nucleosynthesis.

The dynamics of NSBH mergers is profoundly different from the dynamics of binary NS (BNS) mergers (see Nakar 2019 for a review), but their EM counterparts are expected to share some similarities. The mass ejection depends mostly on whether the tidal radius of the NS is larger or smaller than the innermost stable circular orbit (ISCO) of the BH. In the first case, a significant fraction of the NS mass is ejected. A soft EOS of the NS is the main responsibility for a large tidal radius, while the ISCO decreases with smaller BH masses and higher spin component in the binary orbital plane (e.g., Foucart 2012;

Kawaguchi et al. 2015, 2016). If the tidal radius is larger than the ISCO, then as the NS approaches the tidal radius, a 0.01 – $0.1 M_{\odot}$ tidal tail can be dynamically created. These dynamical ejecta have a low electron fraction Y_e , favoring heavy-element production via r -process. An accretion disk can then form around the BH with mass ~ 0.1 – $0.3 M_{\odot}$. About 40% of the disk mass is ejected, constituting a secular ejecta component (e.g., Siegel & Metzger 2018; Fernández et al. 2019). This component may contain polar winds with velocities $0.1c$ – $0.15c$ during an efficient accretion phase, followed by more isotropic, neutron-rich winds with lower velocities. Simulations suggest that Y_e of the secular ejecta is higher than that of the dynamical one, especially along the polar regions, where the ejecta may be free of the high-opacity lanthanides (Christie et al. 2019; Miller et al. 2019).

For comparison, the GW170817 kilonova was found to have a “red” component with mass $M \sim 0.04 M_{\odot}$, likely encompassing both the tidal ejecta and the post-merger disk wind, with velocity $v \sim 0.1c$ (e.g., Kasen et al. 2017). The nature of the blue component of GW170817 is harder to explain; however, polar winds from efficient accretion onto the BH formed during an NSBH merger may result in a similarly blue transient at early times. If the NS is disrupted within the ISCO, the mass of both the dynamical and the disk ejecta is expected to be small, $< 10^{-3} M_{\odot}$, reducing the likelihood of producing any observable EM counterpart.

To help characterize the uncertain nature of EM emission from NSBH mergers, we present deep, synoptic, and red-sensitive limits on the optical/NIR emission from the NSBH merger S190814bv. We obtained the limits from public, multiband observations of the localization region of S190814bv conducted by the Dark Energy Survey GW (DES-GW) Collaboration (Soares-Santos et al. 2019d), who used the Dark Energy Camera (DECam; Flaugher et al. 2015) to tile $>98\%$ of the localization probability roughly 10 times in each of the i and z bands.

Section 2 gives an overview of the GW event, and Section 3 describes the DECam follow-up. Our analysis methods are described in Section 4, and the results of follow-up observations of candidates of interest are presented in Section 5, using a Planck Collaboration et al. (2016) cosmology to compute absolute magnitudes. In Section 6, we quantify the completeness of our galaxy catalogs. In Section 7, we use the limits obtained in the preceding analysis to constrain the ejecta mass, opacity, and viewing angle of S190814bv. The constraints on the ejecta mass are used to characterize the spin and the mass ratio of the progenitor binary. We summarize our results and present concluding remarks in Section 8.

2. S190814bv

The LIGO Scientific Collaboration & the Virgo Collaboration (2019b) detected the GW event S190814bv on 2019 August 14 21:10:39 UT, using four independent pipelines processing data from three GW interferometers (LIGO Hanford, LIGO Livingston, and Virgo) in triple coincidence. The false-alarm rate of the event was 2×10^{-33} Hz, or approximately 1 in 10^{25} yr. The GW event was first classified as “Mass Gap” with $>99\%$ probability. A “mass gap” system refers to a binary where the lighter companion has mass $3 M_{\odot} < M < 5 M_{\odot}$, and no material is expected to be ejected. The classification of S190814bv was revised about 12 hr later (The LIGO Scientific Collaboration & the Virgo Collaboration 2019d) based on new parameter estimation obtained with the LALInference offline analysis pipeline (Veitch et al. 2015; Abbott et al. 2016) to an “NSBH” event with $>99\%$ probability. The refined analysis also indicated that there should be $<1\%$ probability of having disrupted material surrounding the resulting compact object. In this work, we observationally probe the presence of remnant material that could generate an optical/NIR signature (see Section 7) and discuss the results in the context of the NSBH scenario.

LIGO/Virgo alerts with an “NSBH” classification refer to events in which the lighter object has $M \leq 3 M_{\odot}$ and the heavier component has $M \geq 5 M_{\odot}$. The maximum mass of an NS, according to the most extreme viable EOS, is $M_{\text{ns,max}} \approx 2.8 M_{\odot}$ (Özel & Freire 2016). It is thus possible, given the LIGO/Virgo definition of “NSBH,” that GW events classified as “NSBH” may actually be mergers of BHs having $M \geq 5 M_{\odot}$, with lower-mass BHs having $M_{\text{ns,max}} \leq M \leq 3 M_{\odot}$. As the masses of the components of S190814bv are not yet public, we cannot yet comment on this possibility.

S190814bv was localized to 23 deg^2 at 90% confidence. For comparison, the BNS merger GW170817 was localized to 28 deg^2 (Abbott et al. 2017) and then refined to 16 deg^2 (Abbott et al. 2019), and the three GW event candidates including NSs identified during O3 before S190814bv were localized to 7461 deg^2 (S190425z; The LIGO Scientific Collaboration & the Virgo Collaboration 2019a), 1131 deg^2 (S190426c; The LIGO Scientific Collaboration & the Virgo Collaboration 2019c), and 1166 deg^2 (S190510g; LIGO Scientific Collaboration & Virgo Collaboration 2019), with S190510g having a significant probability of being nonastrophysical in origin. The precise localization of S190814bv is largely due to the fact that (1) it was detected with three GW interferometers and (2) it had a favorable location in the sky with respect to the antenna pattern of the detectors.

Despite the small localization area, the GW analysis places S190814bv at the fairly large distance of $267 \pm 52 \text{ Mpc}$ (The LIGO Scientific Collaboration & the Virgo Collaboration 2019d). This corresponds to a volume of $5.26 \times 10^4 \text{ Mpc}^3$ for 90% area and 1σ distance, or a volume of $1.09 \times 10^5 \text{ Mpc}^3$ for 90% area and 2σ distance. The distance probability distribution is broadly Gaussian (although skewed) pixel by pixel, but not over the whole map, generally. The S190814bv skymap is relatively small, so the effect is less evident than for larger skymaps, where a pixel-by-pixel approach is particularly appropriate. We focus the analysis presented in this paper on the 2σ volume, corresponding to the redshift range $0.037 < z < 0.081$.

3. Data Set

S190814bv was initially classified as a “mass gap” event, where both the more massive object and the lighter companion are likely BHs. Therefore, S190814bv was considered a suitable candidate for DECam follow-up under the NOAO program ID 2019B-0372 (PI Soares-Santos), which conducts observations of binary BH mergers, with the resulting data becoming immediately public. The program was triggered within a few hours of the merger, before the refined classification issued by The LIGO Scientific Collaboration & the Virgo Collaboration (2019d). The first exposure was taken roughly 7 hr after the merger at UTC 2019 August 15 06:32:43. Data were acquired on six distinct Chilean calendar nights (2019 August 14, 2019 August 15, 2019 August 16, 2019 August 17, 2019 August 20, and 2019 August 30), lasting from 1.5 to 4.5 hr each night. The moon and weather conditions steadily improved between the first and the last nights of the run, and the exposure times were more than twice as long in each filter at the end of the run than the beginning, resulting in a greater achieved depth. Figure 1 shows the locations of the DECam exposures obtained during the run and processed in this analysis relative to the LALInference skymap of S190814bv.

4. Methods

We processed the raw DECam data as they were taken, using the pipeline described in Goldstein et al. (2019b), now running on the Amazon Web Services Elastic Compute Cloud (EC2) for increased reliability. For each exposure, a `c5.18xlarge` spot EC2 instance with 72 vCPUs and 144 GB of RAM was launched to astrometrically and photometrically calibrate the DECam CCD images in parallel, make references, perform subtractions, identify candidates, filter them using `autoScan` (Goldstein et al. 2015), and perform aperture photometry. Each exposure took roughly 20 minutes to process, and the results were stored on the Amazon Simple Storage Service (S3). The median depths achieved nightly during the follow-up campaign with DECam are presented in Table 1.

4.1. Photometric Redshifts

At the distance to S190814bv ($\sim 250 \text{ Mpc}$), spectroscopic redshift catalogs are largely incomplete (Dálya et al. 2018, D. Cook et al. 2020, in preparation). We therefore relied primarily on photometric redshifts of transient host galaxies to assess whether transient candidates had distances consistent with the GW distance of S190814bv. We carried out an offline analysis of the DESI Legacy Imaging Surveys (Dey et al. 2019) Data Release 8 (DR8), which includes model-based photometry from the DECam and from the *Wide-field Infrared Survey Explorer* (WISE; Wright et al. 2010), to estimate photometric redshifts for the galaxies in the S190814bv localization region. By applying a Random Forest algorithm to the DR8 data (Zhou et al. 2019, in preparation), we generated a photometric redshift catalog for the entire DR8 footprint.

Due to its inclusion of data from DES (Dark Energy Survey Collaboration et al. 2016) observations, the catalog fully covered the S190814bv localization region. Cataloged sources with $m_z > 21$ were excluded because beyond that threshold the accuracy of the photometric redshifts rapidly degraded. As explained in Section 6, the impact of restricting our attention to

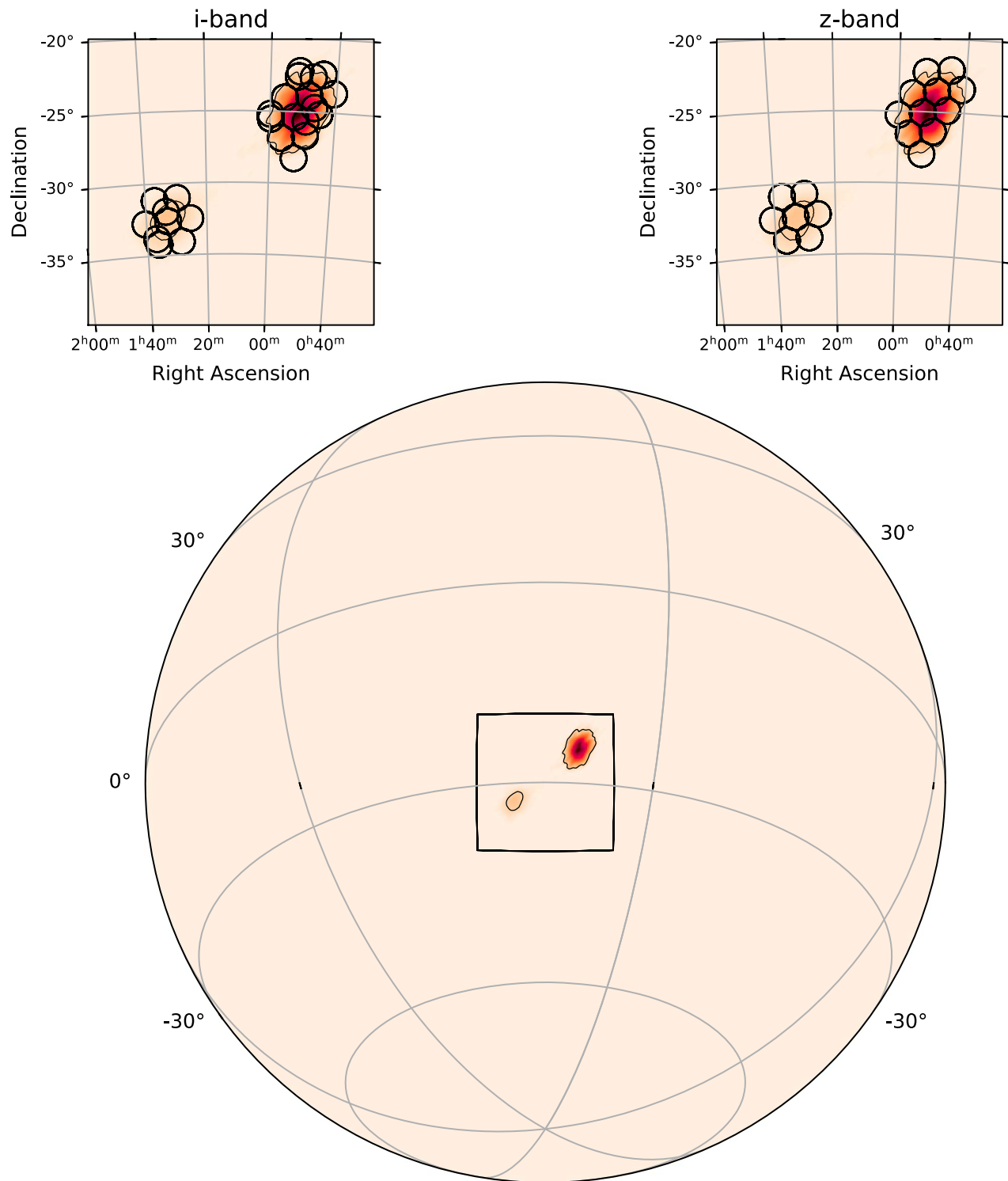


Figure 1. Top row: locations of DECam exposures processed in this analysis (black circles) relative to the S190814bv LALInference skymap (The LIGO Scientific Collaboration & the Virgo Collaboration 2019d), with color linearly proportional to localization probability density. Bottom row: bounding box of the top two panels (black square) relative to a global projection of the LALInference skymap.

candidates with potential host galaxies brighter than $z = 21$ has a negligible impact on our completeness, with an expected loss in luminosity fraction of $< 3\%$.

Sources with photometric redshift uncertainties $> 2 \times$ the average photometric redshift uncertainty of all the sources of a similar magnitude within a 1 deg radius (± 0.1 mag) were also

excluded as potential hosts. The distribution of photometric redshift uncertainties was estimated after rejecting stellar sources using a cut on the morphology of the best-fit light profile. We also rejected sources with *Gaia* parallaxes that are not compatible with 0 ± 1.081 mas obtained from the analysis of parallaxes measured for quasars (Luri et al. 2018). Spectroscopic redshifts (primarily

Table 1
Median Depth Achieved during the Follow-up of S190814bv

Average Date (UT)	Δt (days)	$m_{lim,i}$ 5 σ -phot	$m_{lim,z}$ 5 σ -phot	$m_{lim,i}$ Detection Limit	$m_{lim,z}$ Detection Limit	P_{enc} (i)	P_{enc} (z)	P_{enc} ($i+z$)
2019 Aug 15 08:18	0.46	21.1	20.9	20.4	20.3	92%	94%	94%
2019 Aug 16 07:57	1.45	21.8	22.0	21.0	21.1	97%	97%	98%
2019 Aug 17 06:59	2.41	22.3	22.3	21.3	21.4	97%	97%	98%
2019 Aug 18 07:32	3.43	22.9	22.9	22.1	22.3	97%	97%	98%
2019 Aug 21 06:21	6.38	23.4	23.2	22.8	22.6	93%	93%	94%
2019 Aug 31 06:11	16.37	24.2	...	23.4	...	63%	...	63%

Note. The dates correspond to the central time between the first and the last epoch acquired on each observing night, and Δt indicates the time lag from the merger time (The LIGO Scientific Collaboration & the Virgo Collaboration 2019b). The photometric depth corresponds to 5 σ photometric magnitude limits (Columns (3) and (4)), and detection depth indicates the detection limit of the image-subtraction pipeline. All magnitudes are calibrated to the AB system. The last three columns present the integrated probability of the S190814bv LALInference skymap observed on each observing night, with the last column considering the observations in either i or z filters.

from the 2dF Galaxy Redshift Survey; Colless et al. 2001) were considered instead of photometric redshifts when available.

4.2. Candidate Selection

We used the GROWTH Marshal (Kasliwal et al. 2019) to display, filter, and assess candidates detected with our image-subtraction pipeline. During the scanning process, 519 candidates were saved that were located inside the 95% probability area of the skymap.

The candidates were cross-matched to known solar system objects from the IAU Minor Planet Center using the `astcheck`³⁸ utility. The cross-match radius between candidates and known solar system objects was 100". In addition to excluding known asteroids from our transient list, we identified elongated candidates (likely to be fast-moving uncataloged solar system objects) by visual inspection and removed them.

The selection criteria for candidates to be reported in this work were defined as follows:

1. No match with moving objects reported in the IAU Minor Planet Center.
2. At least two detections in any filter with a time baseline of ≥ 30 minutes to further reject fast-moving objects.
3. Location within the 95% probability contour of the LALInference skymap.
4. The distance to a possible host must be consistent with the distance range expected for S190814bv (accounting for $2\times$ the standard deviation of the distance probability distribution, which translates into a redshift range of $0.037 < z < 0.081$). The distance to host galaxies was obtained from spectroscopic or photometric redshifts available before dedicated follow-up. For the photometric redshifts, we required a host luminosity $m_z < 21$ (see Section 4.1), and, to be more conservative, we considered $2\times$ the uncertainty on the photometric redshifts.
5. At least three detections with an `autoScan` classification score > 0.3 to reject image-subtraction artifacts (see Section 4).
6. At least 10 DECam visits (including nondetections) obtained with observations on different nights, with different filters, and as a result of the dithering pattern used on individual nights in each filter. Most coordinates on the skymap had at least 20 visits (see Figure 1).

Candidates discovered in real time were reported to the Transient Name Server.³⁹ New candidates (Andreoni et al. 2019; Goldstein et al. 2019c, 2019a) and transient follow-up were reported via Gamma-ray Coordinates Network (GCN) circulars during the follow-up campaign. We used a radius of 20" to cross-match our candidates with the photometric redshift catalog (see Section 4.1), which corresponds to a physical distance of 16 kpc at $z = 0.037$ and of 36 kpc at $z = 0.081$. A total of 21 candidates survived the cuts. The candidates passing the selection criteria are listed in Tables 2 and 3.

4.3. Candidate Follow-up Methods

The spectroscopic results presented in this paper include data obtained using the Near Infrared Echelle Spectrometer (NIRES) and the Low Resolution Imaging Spectrometer (LRIS; Oke et al. 1995) at the W. M. Keck Observatory. The NIRES data were reduced using the `spectool` code (Cushing et al. 2004) adapted for NIRES. The LRIS data were processed using `lpipe`, the fully automated reduction pipeline for long-slit spectroscopy described in Perley (2019). We observed three potential candidates with the 10.4 m Gran Telescopio de Canarias (GTC; PI A. Castro-Tirado), located at the observatory of Roque de los Muchachos in La Palma (Canary Islands, Spain), equipped with the Optical System for Imaging and low-intermediate-Resolution Integrated Spectroscopy (OSIRIS; Cepa et al. 2000). GTC/OSIRIS spectra for the three targets were obtained with either the R1000B or R1000R grisms and a 1" slit covering the 3700–7500 Å or 5100–10000 Å range. The slit was placed in order to cover the candidate location and the host galaxy center. Data were reduced and calibrated using standard routines. Optical images in the r -band filter were also taken for the candidates with GTC. Photometric zero-points and astrometric calibration were computed using the Pan-STARRS catalog (Chambers et al. 2016). We then performed point-spread function matching photometry of the targets. Spectroscopy of one candidate of interest was also obtained with the 10 m Southern African Large Telescope (SALT; Buckley et al. 2006, PI Buckley) equipped with the Robert Stobie Spectrograph (RSS; Burgh et al. 2003; Kobulnicky et al. 2003). The primary data reduction of the SALT/RSS spectrum was done using the `PySALT` package (Crawford et al. 2010), which accounts for basic CCD characteristics (e.g., cross-talk, bias and gain correction) and cosmic-ray removal. Standard IRAF/Pyraf routines were then used to undertake wavelength and relative

³⁸ <https://www.projectpluto.com/astcheck.htm>

³⁹ <https://wis-tns.weizmann.ac.il>

Table 2
Subset of Candidates Discovered or Independently Detected by the DECam-GROWTH Team during the Follow-up of S190814bv That Were Spectroscopically Classified

Name	IAU Name	R.A. (deg)	Decl. (deg)	Offset (arcsec)	spec-z	Classification	References
DG19qabkc	AT2019nqc	22.265296	-32.705155	2.2	0.078 ± 0.001	SN II	Andreoni et al. (2019); Buckley et al. (2019); Lopez-Cruz et al. (2019a); Herner et al. (2019a); Dichiara et al. (2019a); Goldstein et al. (2019c); De et al. (2019d); Dichiara et al. (2019b); Evans et al. (2019); D’Avanzo et al. (2019)
DG19wxnjc	AT2019npv	13.384653	-23.832918	2.1	0.056	SN Ibc	Goldstein et al. (2019a); De et al. (2019b); Gomez et al. (2019); Herner et al. (2019b); Evans et al. (2019); Jonker et al. (2019); Smartt et al. (2019); Chen et al. (2019); Annis et al. (2019); Fremling et al. (2019); De et al. (2019c); Palmese et al. (2019); Dobie et al. (2019); Lipunov et al. (2019); Coughlin et al. (2019a); Mooley et al. (2019); Gomez et al. (2019); Wang et al. (2019)
desgw-190814j	AT2019nxe	11.570153	-24.372559	1.9	0.0777	SN Ia	Soares-Santos et al. (2019a); Castro-Tirado et al. (2019); Soares-Santos et al. (2019c)
DG19rzhoc	AT2019num	13.881677	-22.969021	1.9	0.113	SN II	Goldstein et al. (2019a); Herner et al. (2019b); Evans et al. (2019); Dichiara et al. (2019c); Fremling et al. (2019); Tucker et al. (2019b); Corre et al. (2019); Yang et al. (2019)
PS19epf	AT2019noq	12.199507	-25.306523	5.0	0.07	SN II	Huber et al. (2019); Rodríguez et al. (2019)
DG19wgmjc	AT2019npw	13.968326	-25.783301	1.3	0.163	SN Iib	Andreoni et al. (2019); Dichiara et al. (2019a); Goldstein et al. (2019c); De et al. (2019d); Dichiara et al. (2019b); Herner et al. (2019b); Evans et al. (2019); Fremling et al. (2019); Tucker et al. (2019b); Corre et al. (2019); Yang et al. (2019)
DG19sbzkc ^a	AT2019ntr	15.007883	-26.714390	11.6	0.2	SN II	Goldstein et al. (2019a); Goldstein & Anand (2019); Dichiara et al. (2019c); Soares-Santos et al. (2019c); Wiesner et al. (2019b); Corre et al. (2019); Yang et al. (2019)
desgw-190814q	AT2019obc	14.566689	-24.139699	1.4	0.216 ± 0.005	SN Ia	Soares-Santos et al. (2019b); Fremling et al. (2019); Soares-Santos et al. (2019c); Castro-Tirado et al. (2019)
ZTF19abkfmjp	SN2019mbq	10.835364	-25.883974	1.0	0.104 ± 0.013	SN II	Soares-Santos et al. (2019d); Yang et al. (2019)

Note. None of them is a viable optical counterpart to S190814bv. The reported candidates passed the selection criteria described in Section 4.2. Specifically, they lie within the 95% probability region of the LALInference skymap and are within 20'' from galaxies whose redshifts (2σ uncertainty) are compatible with the LIGO/Virgo distance (2σ). All the transients reported in this table were detected using the image-subtraction pipeline described in Section 4.

^a We note that DG19sbzkc was observed with <10 visits and was added to this table for completeness.

Table 3Additional Candidates Discovered during the Follow-up of S190814bv, Whose Host Galaxy Redshift Is Compatible with the LIGO/Virgo Distance (2σ)

Name	IAU Name	R.A. (deg)	Decl. (deg)	Offset (arcsec)	z_{phot}	σ_z	$\langle m_i - m_z \rangle$	$\langle \dot{m}_i \rangle$ (mag day $^{-1}$)	$\langle \dot{m}_z \rangle$ (mag day $^{-1}$)
DG19aferc	AT2019tig	14.517916	-26.083013	0.08	0.074	0.03	...	-0.01	...
DG19gxuqc	AT2019paa	13.807414	-24.119017	0.40	0.116	0.06	0.01	-0.09	0.09
PS19ek ^a	AT2019nbp	11.739110	-24.361751	0.42	0.102	0.01	-0.18	0.01	0.03
DG19hqhjc	AT2019nuj	12.257212	-23.234668	0.25	0.074	0.12	0.01	-0.01	0.00
DG19ilqnc	AT2019tih	11.861086	-27.600835	14.41	0.217	0.08	...	0.03	...
DG19kpykc	AT2019nul	13.818560	-26.943068	0.44	0.095	0.01	-0.23	-0.07	-0.09
DG19tedsc	AT2019tii	12.396721	-27.035924	0.21	0.055	0.03
DG19wynuc	AT2019tij	12.232094	-22.393476	0.32	0.157	0.11	0.43	-0.06	-0.02
DG19bpkf	AT2019tiw	15.022907	-24.950557	0.70	0.218	0.07	...	0.01	...
DG19bown	AT2019tix	12.190325	-24.647386	4.27	0.190	0.07	-0.14	0.02	0.01
DG19ggesc	AT2019paw	12.142854	-25.090528	19.47	0.285	0.13	0.23	0.00	0.03
DG19zoonc	AT2019nyy	12.069377	-26.640810	11.52	0.212	0.07	-0.01
DG19gyvx	AT2019thm	11.985939	-26.900779	18.73	0.233	0.09	0.03

Note.^a DG19hcsge, with Pan-STARRS1 pre-discovery on 2019 August 09.

flux calibrations. Due to the design of SALT, which has a changing field-dependent entrance pupil, spectrophotometric standard observations can only provide relative fluxes (Buckley et al. 2018).

The photometric evolution of the most promising candidates was monitored using the optical imaging component of the Infrared-Optical suite of instruments (IO:O) on the 2 m Liverpool Telescope (LT; Steele et al. 2004) at Observatorio del Roque de los Muchachos. All images were processed with the LT IO:O pipeline, and image subtraction was performed automatically using Pan-STARRS (Chambers et al. 2016) imaging as a reference, using the methods described in Fremling et al. (2016). Optical photometric follow-up data were also acquired using the Las Cumbres Observatory (LCO) telescope network under proposal ID 2019B-0244 (PI Coughlin). The LCO photometry was measured after subtracting reference images from the Legacy Surveys archive using the HOTPANTS package (Becker 2015). At infrared wavelengths we obtained photometry using the Wide-field Infrared Camera (WIRC; Wilson et al. 2003) on the Palomar 200-inch Hale telescope (P200). The P200/WIRC data were reduced using a reduction pipeline developed by members of our team (K. De et al. 2020, in preparation).

5. Results

In this section, we describe the follow-up observations that were conducted to characterize each of the 21 objects that we selected as candidate counterparts to S190814bv using the methods described in Section 4. In addition, we discuss a selection of candidates that did not pass our selection criteria but that were reported and extensively followed up in the first 3 weeks after S190814bv. Most of the objects presented individually were spectroscopically classified.

DG19qabkc/AT2019nqc.—The candidate was first reported in Andreoni et al. (2019) and appeared to be $\sim 2''$ offset from its host galaxy. Although no spectroscopic redshift was available, the photometric redshift placed the host in the correct distance range (Goldstein et al. 2019c). The candidate was photometrically confirmed in the optical (Dichiara et al. 2019a, 2019b; Herner et al. 2019a), and we detected the transient in the NIR at magnitude $J \sim 21.4 \pm 0.2$ on 2019 August 18 using P200/WIRC (De et al. 2019d). A flux upper limit of $F < 2.9 \times 10^{-12}$ erg cm $^{-2}$ s $^{-1}$

(Evans et al. 2019) was placed using data acquired with the X-ray Telescope (XRT; Burrows et al. 2005) on the space-based *Neil Gehrels Swift Observatory*, hereafter referred to as *Swift*. We observed DG19qabkc/AT2019nqc with SALT/RSS starting on 2019 August 23 22:46:10, and two consecutive 1200 s exposures were obtained using the PG300 transmission grating, which covered the spectral region 3300–9800 Å. The seeing was $\sim 1''.7$, and a $1''.5$ slit was used, giving an average resolving power of ~ 370 , or a resolution of ~ 18 Å. A strong broad H α line with a P Cygni profile dominates the spectrum, with a weak H β line in absorption, consistent with a redshift of $z = 0.077$. A good match was obtained using SNID (Blondin & Tonry 2007) using SN2005cs, a Type II supernova (SN II), 14 days after maximum (Figure 2; see also Buckley et al. 2019). Our GTC/OSIRIS spectroscopic observations confirmed DG19qabkc/AT2019nqc to be an SN II at $z = 0.078 \pm 0.001$ (Lopez-Cruz et al. 2019a). We extensively monitored the transient with LCO and LT imaging. The photometry that we obtained (data behind Figure 3) confirms a slow evolution compatible with SN behavior.

DG19wxnjc/AT2019npv.—When the candidate was discovered (Goldstein et al. 2019a), it appeared to be offset from its host galaxy, the photometric redshift of which ($z = 0.072 \pm 0.056$) was compatible with the expected distance to S190814bv. The redshift of the host was spectroscopically measured to be $z = 0.056$ (Jonker et al. 2019). The candidate was later confirmed in the optical and NIR (Chen et al. 2019; Herner et al. 2019b; Lipunov et al. 2019; Smartt et al. 2019; Wang et al. 2019), but no X-ray counterpart was detected with *Swift*/XRT ($F < 3.8 \times 10^{-12}$ erg cm $^{-2}$ s $^{-1}$; Evans et al. 2019), and no radio counterpart was detected with the Australian Square Kilometre Array Pathfinder ($S_{943 \text{ MHz}} < 75 \mu\text{Jy}$; Dobie et al. 2019) and Karl G. Jansky Very Large Array ($S_{6 \text{ GHz}} < 12 \mu\text{Jy}$; Mooley et al. 2019). Palmese et al. (2019) reported a possible archival detection in DES data, questioning the transient nature of DG19wxnjc/AT2019npv. Annis et al. (2019) produced precise photometry obtained with nightly stacks of DECam data, indicating the transient to be reddening at a rate $\Delta(i - z) \sim 0.05$ mag day $^{-1}$. The transient was also monitored photometrically with LCO and LT (see Coughlin et al. 2019a and data behind Figure 3), which produced detections in the r , i , and z bands and a marginal detection $g \gtrsim 23.0$ on 2019 August 24 with LCO, further indicating the transient to be (or to have become) red in color. We

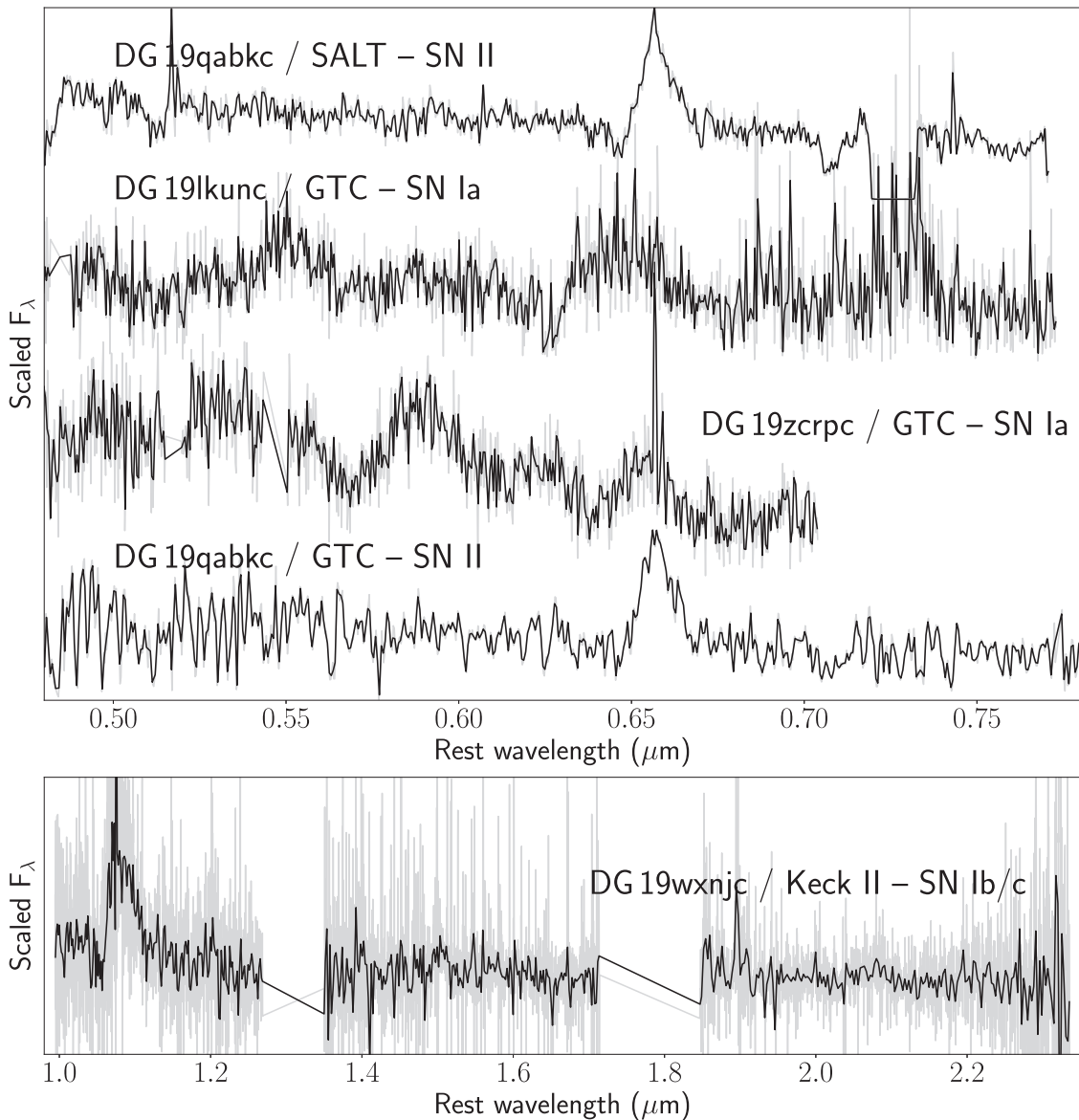


Figure 2. Top panel: optical spectroscopic follow-up of candidates found in the localization region. The black lines correspond to binned versions of the unbinned reduced spectra shown in gray. GTC/OSIRIS and SALT spectra of DG 19qabkc show a strong P Cygni H α line suggesting an SN II at $z = 0.08$. GTC/OSIRIS spectra of DG19lkunc and DG19zcrpc are consistent with SNe Ia at $z = 0.21$ and $z = 0.08$, respectively. Bottom panel: NIR spectrum of DG19wxnjc obtained with Keck II/NIRES. The spectrum shows a prominent P Cygni feature at $\approx 1.08 \mu\text{m}$, consistent with He I with an absorption velocity of 7000 km s^{-1} , classifying this source as an SN Ib/c. These classifications rule out associations of these sources with S190814bv.

obtained one epoch of P200/WIRC imaging of the transient in J band and did not detect the source to a 5σ limit of 21.4 AB mag, although we caution that the photometry is contaminated by host galaxy light.

We obtained one NIR spectrum of DG19wxnjc with NIRES on the Keck II telescope on 2019 August 24 (De et al. 2019c, 2019b). We acquired two sets of dithered ABBA exposures on the transient location for a total exposure time of 40 minutes. The telluric standard HIP 7202 was used for flux calibration. The reduced and stacked spectra showed a largely featureless continuum between 1.0 and 2.5 μm (Figure 2), along with a prominent P Cygni profile near 1.08 μm with an absorption velocity of $\approx 7000 \text{ km s}^{-1}$. This feature is consistent with He I at the redshift of the host galaxy, in addition to a weak hint for another He I feature at 2.05 μm , confirming the classification of this source as an SN Ib/c and unrelated to S190814bv. Gomez et al. (2019) confirmed the SN Ib

classification using the IMACS optical spectrograph on the Magellan telescope.

desgw-190814j/AT2019nxe.—The candidate was announced by Soares-Santos et al. (2019a) and was independently detected with our image-subtraction pipeline on multiple z -band epochs with internal name DG19zcrpc. The photometric redshift of the host is $z = 0.106 \pm 0.035$. LCO photometry (data behind Figure 3) suggests no significant g -band evolution between 2019 August 22 and 2019 August 25 and color $r - i \approx 0$ on 2019 August 22. The transient was observed with GTC in imaging and spectroscopy mode on 2019 August 23. The GTC/OSIRIS spectrum of *desgw-190814j/AT2019nxe* is compatible with an SN Ia at redshift $z = 0.0777 \pm 0.0005$ (Castro-Tirado et al. 2019).

DG19rzhoc/AT2019num.—We identified this candidate in DECam data (Goldstein et al. 2019a), and it was independently confirmed in the same data set (Hemer et al. 2019b), in images

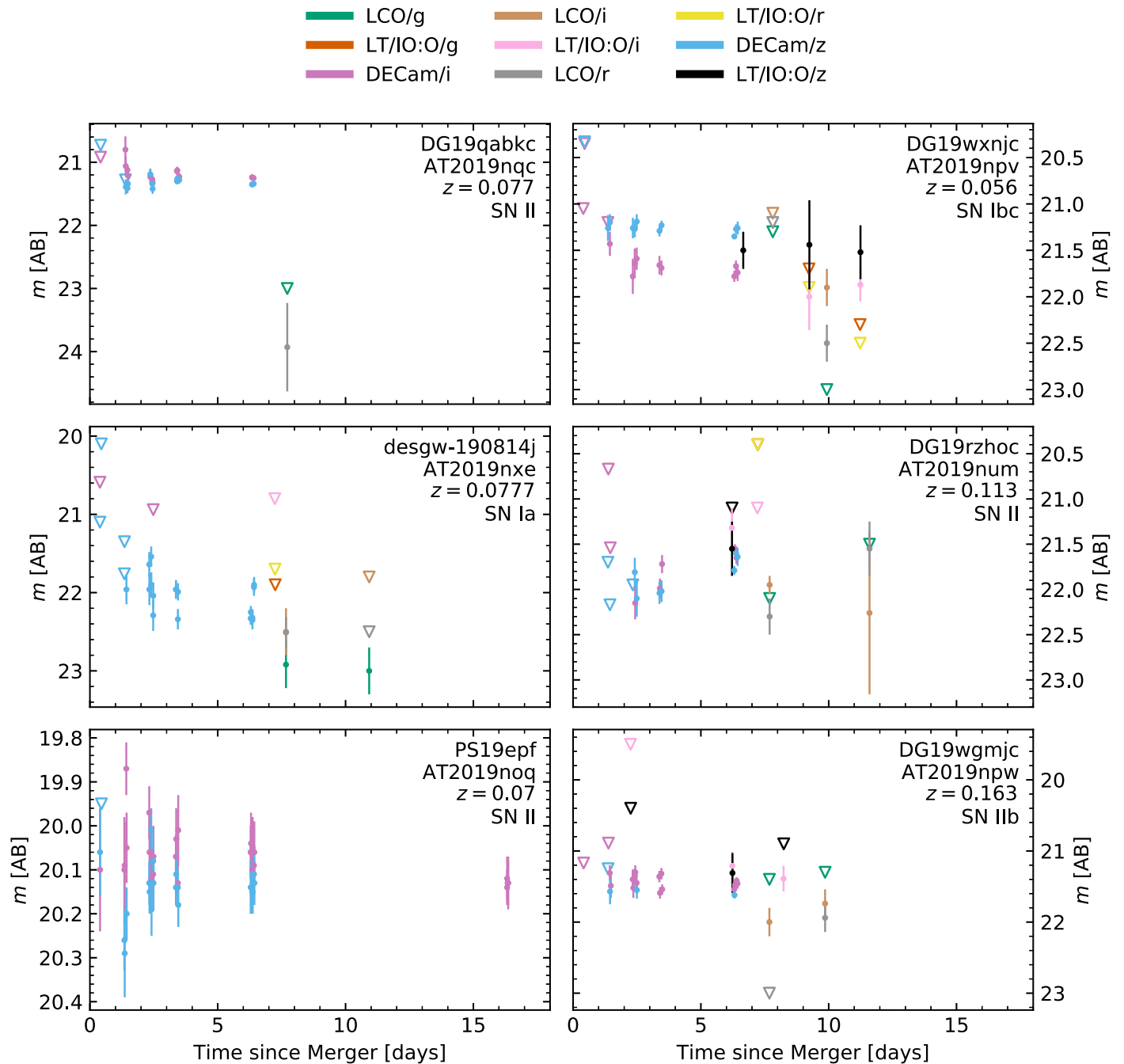


Figure 3. Light curves of the first six candidates presented in Table 2. The LCO and LT photometry upper limits are quoted to 3σ , while DECam upper limits are quoted to 5σ . P200/WIRC photometry was not plotted because it is host contaminated. Photometry for all candidates in Tables 2 and 3 is available in machine-readable form online (data behind the figure). We note that absolute magnitudes were not K -corrected and must be considered to be indicative values.

(The data used to create this figure are available.)

taken with the Reionization and Transients Infrared Camera (RATIR) on the 1.5 m Harold Johnson Telescope at the Observatorio Astronómico Nacional on Sierra San Pedro Martir (Dichiara et al. 2019c) and in VLT Survey Telescope (VST) images (Yang et al. 2019). We performed photometric follow-up with LCO and LT (data behind Figure 3), which revealed the transient to be slowly evolving on day timescales. A *Swift*/XRT upper limit was placed at $F < 4.1 \times 10^{-12} \text{ erg cm}^{-2} \text{ s}^{-1}$ (Evans et al. 2019). We obtained one epoch of P200/WIRC imaging of the source in J band and did not detect the source to a 5σ limit

of 21.4 AB mag, although we caution that the transient location is contaminated heavily with host galaxy light. DG19rzhoc/AT2019num was spectroscopically classified as an SN II at redshift $z=0.113$ using the Goodman High Throughput Spectrograph (GHTS) on the 4.1 m Southern Astrophysical Research (SOAR) telescope (Tucker et al. 2019b).

PS19epf/AT2019noq.—The candidate was identified with the Pan-STARRS1 telescope and reported on 2019 August 15 (Huber et al. 2019). We independently detected PS19epf/AT2019noq in DECam data starting on 2019 August 15 06:44:29 with internal

name DG19lsugc. The transient was classified as an SN II at redshift $z = 0.07$ using SOAR/GHTS (Rodríguez et al. 2019). A pre-detection of the transient in ZTF data 2 weeks before the GW event further excluded its association with S190814bv.

DG19wgmjc/AT2019npw.—This candidate was discovered in DECam data (Andreoni et al. 2019) and flagged as a high-priority target because of the photometric redshift of the putative host $z = 0.140 \pm 0.054$ being compatible with the distance of S190814bv (Goldstein et al. 2019c). The transient was confirmed with optical observations with other telescopes, such as the Discovery Channel Telescope (Dichiara et al. 2019a, 2019b) and VST (Yang et al. 2019), and with our P200/WIRC imaging observations (De et al. 2019d). Photometric measurements on DECam data indicated no rapid optical evolution (Fremling et al. 2019). A *Swift*/XRT upper limit was placed at $F < 4.3 \times 10^{-12}$ erg cm⁻² s⁻¹ (Evans et al. 2019). DG19wgmjc/AT2019npw was eventually classified as an SN IIb at redshift $z = 0.163$ using SOAR/GHTS (Tucker et al. 2019b).

DG19sbzkc/AT2019ntr.—We initially identified this candidate in DECam data (Goldstein et al. 2019a), and the detection was confirmed using RATIR (Dichiara et al. 2019c) and VST (Yang et al. 2019). We note that this transient did not pass the stricter selection criteria adopted in this work (see Section 4.2) because its location was visited 5 times, less than the 10-visit threshold that we imposed. DG19sbzkc/AT2019ntr was spectroscopically classified as an SN II at redshift $z = 0.2$ using SOAR/GHTS (Wiesner et al. 2019b).

desgw-190814q/AT2019obc.—The candidate was found and announced by the DES-GW team (Soares-Santos et al. 2019b), and we independently detected it with our automatic pipeline from 2019 August 16 05:56:59 with internal name DG19lkunc. Our DECam photometry using Pan-STARRS1 templates was consistent with a flat evolution until 2019 August 21 (Fremling et al. 2019). We acquired P200/WIRC NIR imaging in K_s band on MJD 58,717.492, and the transient was not detected down to a 5σ limit of $K_s > 20.72$ AB mag. desgw-190814q/AT2019obc was classified as an SN Ia a few days past its peak at redshift $z = 0.216 \pm 0.005$ using GTC/OSIRIS (Castro-Tirado et al. 2019).

ZTF19abkfmjp/SN2019mbq.—The transient was discovered with ZTF on 2019 July 30 (Nordin et al. 2019), before S190814bv, and it was classified as an SN II at redshift $z = 0.104 \pm 0.013$ with the spectral energy distribution Machine (Blagorodnova et al. 2018) on the 60-inch telescope at Palomar Observatory. We automatically found the transient (dubbed DG19fcmgc) in DECam data, and it was also reported by two other groups via GCN (Soares-Santos et al. 2019d; Yang et al. 2019). Given the pre-detection with ZTF and the SN classification, ZTF19abkfmjp/SN2019mbq cannot be associated with S190814bv.

DG19gxuqc/AT2019paa.—We obtained a spectrum of this nuclear candidate with Keck/LRIS. The spectrum was host dominated, with common emission lines from the galaxy that allowed us to place the host at redshift $z = 0.191$, beyond the acceptable distance range for S190814bv.

All candidates in Table 3 are ruled out based on their photometric evolution being slower than 0.1 mag day⁻¹. This limit was adopted based on the photometric evolution of GW170817, the best-studied kilonova to date. GW170817 faded faster (almost 2 mag in g in 24 hr) and reddened faster (from

$g - z = -0.3$ to $+1.3$ in 24 hr) than any known or theorized transient (e.g., Drout et al. 2017; Cowperthwaite et al. 2017; Kasliwal et al. 2017; Kilpatrick et al. 2017). Theoretical models (e.g., Tanaka et al. 2018; Bulla 2019; Hotokezaka & Nakar 2019) also suggest that kilonovae arising from mergers with at least one NS are rapidly evolving transients. Requiring a photometric evolution faster than 0.1 mag day⁻¹ to be considered a counterpart candidate is thus conservative, corresponding to evolution more than an order of magnitude slower than GW170817.

Other transients were published via GCN circulars but were not reported in Tables 2 and 3 because they did not pass our selection criteria or they were not detected with our pipeline. Soares-Santos et al. (2019c) published a complete list of candidates that they identified in DECam data in the first five nights of observations, including candidates identified in deep nightly stacks. In addition to a number of candidates already discussed in this section, we can associate only two more candidates with galaxies with photometric redshifts compatible with the distance to S190814bv. In particular, DG19zujoc/2019oac is located outside the 95% probability area of the LALInference skymap, and desgw-190814z/AT2019omx did not have enough visits to pass our selection criteria (Section 4.2). In the available epochs, we do not measure any significant variability. Its photometric redshift of $z = 0.21 \pm 0.07$ passed our selection because we considered twice the uncertainties on photometric redshifts; however, its large value suggests that the host galaxy is well beyond the distance range of interest.

Three DECam candidates DG19zoonc/AT2019nyy, DG19gyvx/AT2019thm, and DG19ggesc/AT2019paw lie within a 20'' radius from galaxies with photometric redshift compatible with S190814bv; however, underlying galaxies at larger redshifts are most likely their host. DG19ggesc/AT2019paw is also coincident with a red stellar source detected with VISTA (Greggio et al. 2014). Therefore, we exclude that DG19zoonc/AT2019nyy, DG19gyvx/AT2019thm, or DG19ggesc/AT2019paw is associated with S190814bv.

Two objects labeled desgw-190814a/AT2019nmd and desgw-190814b/AT2019nme were reported as transients possibly associated with S190814bv (Soares-Santos et al. 2019d). These candidates were followed up with several telescopes whose observations resulted in nondetections (Belkin et al. 2019; Corre et al. 2019; Evans et al. 2019; Huber et al. 2019; McBrien et al. 2019). Querying the IAU Minor Planet Center, we found that desgw-190814a/AT2019nmd is consistent with the known asteroid (297025) 2010 GA33 (De et al. 2019a). Inspection of DECam images allowed us to show that desgw-190814b/AT2019nme is a solar system fast-moving object (Goldstein et al. 2019d) absent from the Minor Planet Center database. In conclusion, both desgw-190814a/AT2019nmd and desgw-190814b/AT2019nme were moving objects unrelated to S190814bv.

The transient labeled desgw-190814d/AT2019nqr was first reported by Herner et al. (2019a). The candidate was detected twice with our automated pipeline (internal name DG19pihic), but the two detections occurred only 2.2 minutes apart on 2019 August 16, too close in time to pass our selection criteria of >30 minutes between the first and last detection. desgw-190814d/AT2019nqr was later classified as an SN IIb using SOAR/GHTS (Tucker et al. 2019a).

The candidate desgw-190814c/AT2019nqq (D’Avanzo et al. 2019; De et al. 2019d; Dichiaro et al. 2019c; Goldstein et al. 2019c; Herner et al. 2019a, 2019b; Tucker et al. 2019a) was automatically detected with our pipeline (dubbed DG19kxqic), but it was not included in Table 2 because it lies outside the LALInference 95% probability area of S190814bv. desgw-190814c/AT2019nqq was classified as an SN II at $z = 0.071 \pm 0.001$ using GTC/OSIRIS (Lopez-Cruz et al. 2019b).

Follow-up observations were performed also for the candidates named desgw-190814f/AT2019nte (Herner et al. 2019b) and desgw-190814r/AT2019odc (Soares-Santos et al. 2019c). The redshifts of their putative host galaxies were fixed to $z = 0.054 \pm 0.001$ for desgw-190814r/AT2019odc (as part of our GTC/OSIRIS observations; Hu et al. 2019) and $z = 0.0702$ from the 2dF Galaxy Redshift Survey. However, both candidates did not pass the quality and reliability checks in our pipeline, in agreement with the nondetection of transient signatures in the spectra.

Four additional candidates that were detected with our pipeline were spectroscopically classified as SNe. The photometric redshift of their putative hosts placed them beyond the distance range for S190814bv. In particular, the spectrum of DG19rtekc/AT2019ntn (Goldstein et al. 2019a) obtained with SOAR/GHTS is consistent with an SN Ia-CSM or an SN IIn at $z = 0.1$ (Rodríguez et al. 2019); the GTC/OSIRIS spectrum of desgw-190814v/AT2019omt (Soares-Santos et al. 2019c) is consistent with an SN II at $z = 0.1564 \pm 0.0005$ (Hu et al. 2019); DG19gcwjc/AT2019ntp (Goldstein et al. 2019a) was classified as a broad-line SN Ic with SOAR/GHTS (Wiesner et al. 2019a); finally, the candidate desgw-190814e/AT2019nqs (Dichiaro et al. 2019a; Herner et al. 2019a) was classified as an SN Ia or SN Ibc at redshift $z = 0.1263$ using the X-shooter instrument on the Very Large Telescope (VLT; Bruun et al. 2019).

In summary, none of the transients unveiled during this follow-up campaign appears to be a viable EM counterpart to the NSBH merger S190814bv.

6. Galaxy Catalog Completeness

The completeness of a synoptic follow-up campaign such as the one conducted with DECam for S190814bv is mainly limited by the area covered and the efficiency of the transient detection pipeline. Once these two quantities are set, the ability to detect an EM counterpart becomes flux limited. Given a mean detection limit of 21.7 mag (Table 1), we were able to find transients with absolute magnitude $M \leq -14.4$ at a distance $D = 163$ Mpc, $M \leq -15.4$ at $D = 267$ Mpc, and $M \leq -16.1$ at $D = 371$ Mpc.

Several publications (e.g., Nissanke et al. 2013; Gehrels et al. 2016; Singer et al. 2016) advocate that galaxy-targeted follow-up of GW triggers can be very effective when the event occurs within tens of megaparsecs. The discovery of AT2017gfo (the optical counterpart to GW170817) using a galaxy-targeted strategy is an example of success of this approach at a distance of 41 Mpc (Coulter et al. 2017). However, at distances beyond ~ 200 Mpc, galaxy-targeted searches become more challenging. Gomez et al. (2019) used the Magellan telescope to observe galaxies possibly hosting the S190814bv merger. In their work, Gomez et al. (2019) imaged 96 galaxies at 3σ magnitude limit $i < 22.2$, corresponding to $M_i = -14.9$ mag at 267 Mpc. The sample includes all galaxies in the GLADE catalog within the 50% probability volume with luminosity $\geq 0.15L^*$.

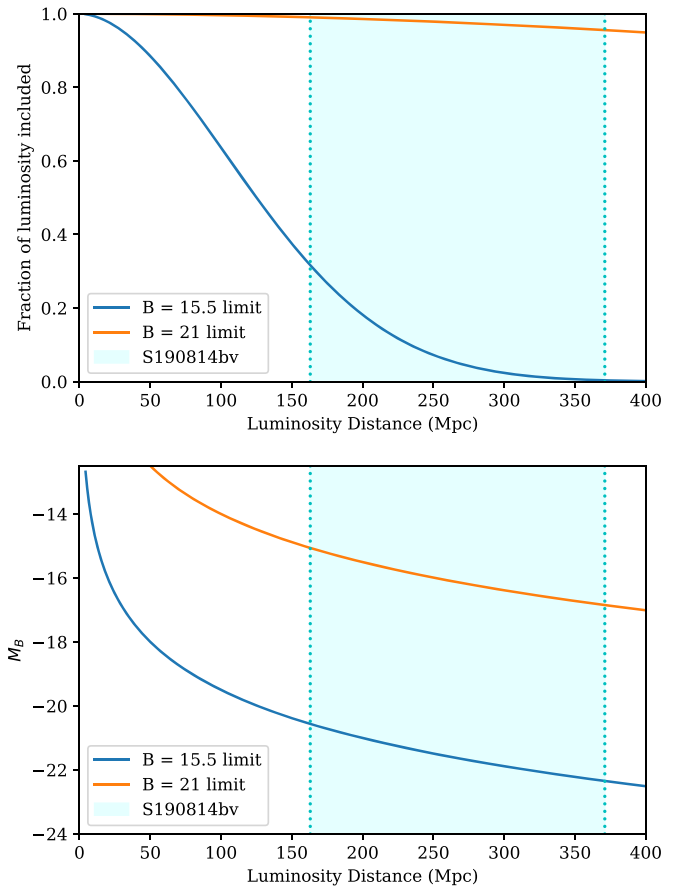


Figure 4. Luminosity fraction (top panel) and B -band absolute magnitude limit (bottom panel) as a function of luminosity distance. These quantities were estimated for the Legacy Surveys DR8 photometric redshifts (orange line), as well as for the Galaxy List for the Advanced Detector Era (GLADE; Dálya et al. 2018; blue line) assuming the catalog to be complete for $B < 21$ and $B < 15.5$ (de Vaucouleurs et al. 1991; Corwin et al. 1994), respectively, using a Schechter function as in Gehrels et al. (2016). The 2σ distance interval for S190814bv (The LIGO Scientific Collaboration & the Virgo Collaboration 2019d) is delimited by the cyan-colored dashed lines.

The analysis presented in this paper took advantage of photometric redshifts calculated from Legacy Surveys and *WISE* photometry mainly to exclude from our sample those candidates likely associated with galaxies significantly outside the distance range of S190814bv. Astrophysical transients with no clear association with a host galaxy were not excluded a priori, but their photometric evolution was not rapid enough for them to be considered likely counterparts to S190814bv. Nevertheless, we estimate the completeness that we could reach considering only a sample of transients found in the proximity of galaxies present in the photometric redshift catalog. Assuming a conservative limit of $B = 21$, we obtain a completeness $>97\%$ based on the luminosity fraction given a Schechter luminosity function (Gehrels et al. 2016) in the 2σ distance range of S190814bv (Figure 4). Although it is likely that the $z < 21$ excludes a large number of small, faint galaxies with $z > 21$, we are still nearly complete in luminosity. We note that z -band luminosity is a much better proxy for stellar mass than luminosity in bluer bands such as B , such that the spread in z -band mass-to-light ratio is smaller than the range of B/z flux ratios among galaxies. As a result, the stellar mass completeness of the $z < 21$ subset of DECaLS would be

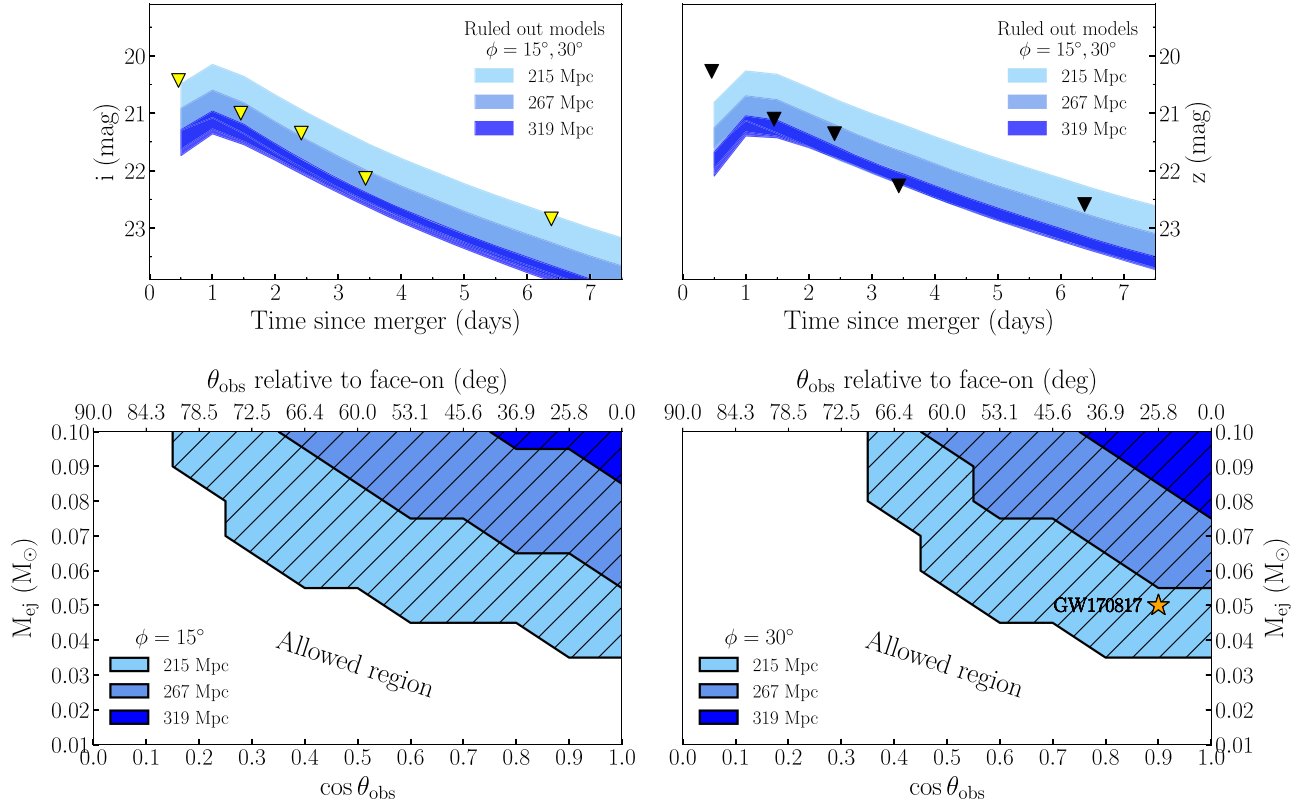


Figure 5. Limits obtained with DECcam observations excluded regions of the parameter space for given kilonova models. In this figure we consider models obtained with the Monte Carlo radiative transfer code POSSIS (Bulla 2019), whose key parameters are the viewing angle θ_{obs} , the half-opening angle of an equatorial lanthanide-rich component ϕ , and the ejecta mass M_{ej} . Top: i -band (left) and z -band (right) light curves of kilonovae ruled out using the multiband DECcam upper limits (Table 1), here marked with triangles. Bottom: using the multiband DECcam upper limits, regions of the ejecta mass and viewing angle parameter space can be ruled out using $\phi = 15^\circ$ (left) and $\phi = 30^\circ$ (right). The best-fit model to GW170817 in this grid ($M_{\text{ej}} = 0.05 M_\odot$, $\phi = 30^\circ$, and $\cos\theta_{\text{obs}} = 0.9$; Dhawan et al. 2020) is marked with a yellow star in the right panel. Both the top and bottom panels show that constraints on the models are more stringent if lower distances to S190814bv are considered. Here we used distances of 319 Mpc (dark-blue patches), 267 Mpc (light-blue patches), and 215 Mpc (cyan patches).

expected to be at least as high as the conservative B luminosity completeness estimated here.

7. Discussion

The results presented in Section 5 show that no viable counterpart to S190814bv was discovered. In this section we discuss the constraints that this nondetection places on the astrophysical properties of the merger if the candidate was originally an NSBH.

7.1. Kilonova Models

We used the upper limits obtained with DECcam and kilonova simulations to constrain the parameter space of the possible EM counterpart to S190814bv. Specifically, we consider the kilonova models developed by Bulla (2019) and Hotokezaka & Nakar (2019).

We first compare DECcam limits to 2D kilonova models computed with the Monte Carlo radiative transfer code POSSIS (Bulla 2019). These models assume a two-component ejecta geometry, with a lanthanide-rich component distributed around the equatorial plane and characterized by a half-opening angle ϕ and a lanthanide-poor component at higher latitudes (see Figure 1 in Bulla et al. 2019). Radiative transfer calculations are then performed to predict spectral time series for 11 different viewing angles, from which broadband light curves can be easily extracted. For our analysis, we choose $\phi = 15^\circ$ and $\phi = 30^\circ$

guided by numerical simulations (Kawaguchi et al. 2016; Fernández et al. 2017) and calculate light curves for ejecta masses M_{ej} between 0.01 and 0.10 M_\odot (step size 0.01 M_\odot).

The top panels of Figure 5 show which modeled light curves are ruled out by DECcam i -band (left) and z -band (right) limits for different distance assumptions (215, 267, and 319 Mpc from light to dark blue). As expected, more models are brighter than the limits and thus ruled out at closer compared to farther distances. Interestingly, we find that the most constraining limit is the z -band point at 3.4 days ($z = 22.3$ mag), with all the other limits bringing no improvement in terms of ruling out models. We note that comparable deep limits at earlier epochs, when the kilonova is intrinsically brighter, would have been extremely important to constrain the parameter space more strongly.

The bottom panels of Figure 5 show what region of the M_{ej} -viewing angle parameter space is ruled out for $\phi = 15^\circ$ (left) and $\phi = 30^\circ$ (right). The brightest kilonovae in the modeled grid are predicted at high M_{ej} and for polar viewing angles (system viewed face-on, $\theta_{\text{obs}} = 0$, and $\cos\theta_{\text{obs}} = 1$). These models are therefore the first to be ruled out by DECcam limits (upper right corner in the M_{ej} -viewing angle parameter space). Stronger constraints are found for closer distances (see above) and smaller ϕ angles, as the larger contribution of the lanthanide-poor compared to lanthanide-rich component leads to an intrinsically brighter kilonova. We note that the best-fit model to GW170817 in this grid ($M_{\text{ej}} = 0.05 M_\odot$, $\phi = 30^\circ$, and

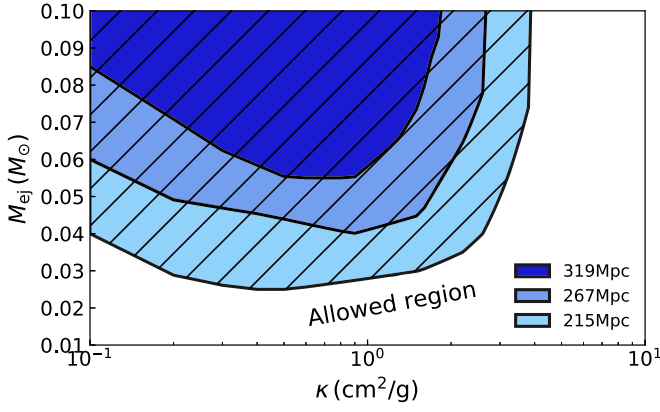


Figure 6. Constraints on the ejecta mass (M_{ej}) and opacity (κ) phase space obtained using multiband DECam upper limits (Table 1) and the kilonova models described in Hotokezaka & Nakar (2019). Similarly to Figure 5, the constraints become more significant assuming lower distances to the merger.

$\cos\theta_{\text{obs}} = 0.9$; Dhawan et al. 2020) would be slightly fainter and thus hidden below DECam limits at 267 Mpc. To summarize, ejecta masses are constrained to $M_{\text{ej}} < 0.04 M_{\odot}$ in the most optimistic case assuming the nearest consistent distance of 215 Mpc, $\phi = 15^{\circ}$, and $\cos\theta_{\text{obs}} = 1$ (face-on). A more conservative constraint ($M_{\text{ej}} \lesssim 0.10 M_{\odot}$) is instead found for farther distances, viewing angles closer to the equatorial plane, and larger ϕ values.

Figure 6 presents upper limits on the ejecta mass obtained using a different approach. We assume a spherical ejecta with a power-law density profile $\rho \propto v^{-n}$ for $v_{\text{min}} < v < v_{\text{max}}$ and calculate the emission using the heating-rate formalism and light-curve modeling described in Hotokezaka & Nakar (2019). The outflow parameters are $v_{\text{min}} = 0.1c$, $v_{\text{max}} = 0.4c$, and $n = 4.5$. The composition that we consider is of r -process elements with atomic mass $85 \leq A \leq 209$ and a solar abundance pattern. The heating-rate calculation includes only β -decay. We assume further that the entire ejecta can be characterized by a single gray opacity parameter κ and vary the value of κ . The shaded regions in the $M_{\text{ej}}-\kappa$ space in Figure 6 are where the light curve is brighter than the upper limits we have for this event. The conclusion from this figure is that the ejecta cannot have more than $\sim 0.05 M_{\odot}$ of ejecta that is not lanthanide-rich at a distance of 267 Mpc, or $\sim 0.03 M_{\odot}$ at an optimistic distance of 215 Mpc. This conclusion is in agreement with the results obtained with the Bulla (2019) kilonova models under favorable ($\theta \lesssim 30^{\circ}$) viewing angles.

7.2. Constraints on the Merging Binary

At present, constraints on the amount of mass ejected by the merger can be translated into approximate constraints on the initial parameters of the possible merging NS and BH (see Coughlin et al. 2019b for a summary of other events during O3a). As a proof of principle, given the mass ratio of the binary $Q = M_{\text{BH}}/M_{\text{NS}}$, the dimensionless component of the initial BH spin aligned with the orbital angular momentum (χ_{aligned}), and the compactness of the NS $C_{\text{NS}} = GM_{\text{NS}}/(R_{\text{NS}}c^2)$, we can conservatively assume that

$$M_{\text{ej}} \gtrsim M_{\text{dyn}} + 0.1(M_{\text{out}} - M_{\text{dyn}}),$$

where M_{out} represents the mass that remains outside of the BH after merger (Foucart 2012; Foucart et al. 2018) and M_{dyn}

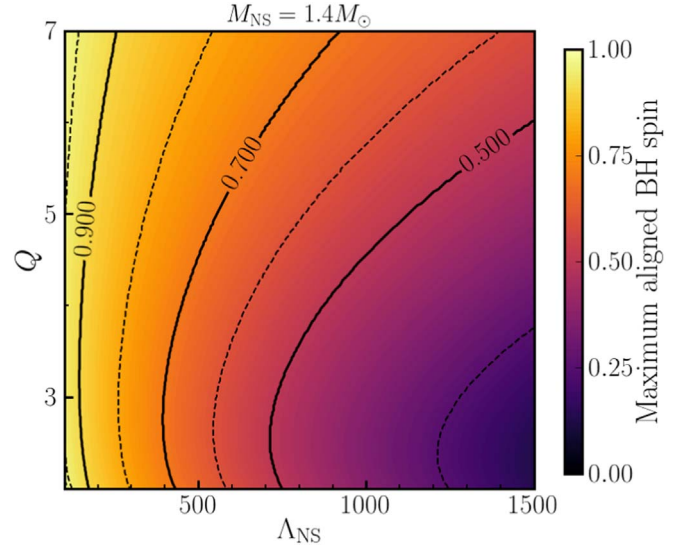


Figure 7. Constraints on the parameter space of BH-NS binaries assuming $M_{\text{ej}} < 0.03 M_{\odot}$. We show the highest possible value of the component of the BH spin aligned with the orbital momentum as a function of mass ratio $Q = M_{\text{BH}}/M_{\text{NS}}$ and tidal deformability Λ_{NS} of the NS. The figure obtained assumes that $M_{\text{NS}} = 1.4 M_{\odot}$, but as the ejected mass is approximately proportional to M_{NS} (at fixed Λ_{NS}), any choice in the range $M_{\text{NS}} - 1.2 - 1.6 M_{\odot}$ would give qualitatively similar constraints.

denotes the mass ejected during disruption (Kawaguchi et al. 2016). Both M_{out} and M_{dyn} are predictions from semianalytical fits to the results of merger simulations. In the above, we have also conservatively assumed that $\gtrsim 10\%$ of the matter initially bound in an accretion disk around the remnant BH will be ejected in magnetically driven and/or neutrino-driven winds, and during viscous expansion of the disk (Fernandez & Metzger 2013; Fernández et al. 2015; Siegel & Metzger 2017; Christie et al. 2019).⁴⁰

In Figure 7, we show constraints on the parameter space of NSBH binaries assuming $M_{\text{ej}} = 0.03 M_{\odot}$.⁴¹ Practically, an upper bound on M_{ej} can be interpreted as a maximum possible value of χ_{aligned} for each choice of mass ratio and dimensionless NS deformability (Q, Λ_{NS}), or an upper bound on Λ_{NS} at fixed χ_{aligned} . Λ_{NS} is related to the NS EOS and is given by $\Lambda_{\text{NS}} = \frac{\lambda c^{10}}{G^4 M_{\text{NS}}^5}$, where $\lambda = 2k_2 R_{\text{NS}}^5/(3G)$ and k_2 is the Love number (see, e.g., Flanagan & Hinderer 2008; Hinderer et al. 2010).

Assuming $\Lambda \sim 800$ (the largest value allowed by GW170817 for a $1.4 M_{\odot}$ NS; Abbott et al. 2017) and $M_{\text{ej}} < 0.03 M_{\odot}$, the data constrain the BH spin component aligned with the orbital momentum to be $\chi < 0.7$ for mass ratios $Q < 6$. This constraint becomes looser for more compact stars (lower Λ) and tighter for less compact stars (larger Λ).

8. Conclusion

In this paper, we have presented deep synoptic limits on the optical counterpart to the NSBH merger S190814bv by

⁴⁰ For low-mass BHs leaving remnants comparable to the initial conditions of existing 3D simulations, $\gtrsim 25\%$ of the disk is most likely ejected, but more compact disks around massive BHs eject a smaller fraction of their disk.

⁴¹ We do not show the conservative case of $M_{\text{ej}} < 0.1 M_{\odot}$, as it does not provide meaningful constraints on the parameter space of the binary because the fitting formulae are not properly calibrated above $\chi_{\text{aligned}} = 0.9$

analyzing publicly available data from a DECam imaging campaign. We identified dozens of counterpart candidates and systematically ruled each of them out using the results of a global follow-up campaign undertaken by our group and the community. Real-time data analysis and prompt follow-up allowed the candidates to be classified at timescales from hours to days. Based on our lack of identification of an optical counterpart, we used our detection limits and kilonova models to constrain the allowable parameter space for S190814bv. We found that the ejecta mass can be poorly constrained at the far end of the distance probability distribution; however, limits on the ejecta mass of $M_{\text{ej}} \lesssim 0.05 M_{\odot}$ can be placed at a luminosity distance of 267 Mpc at polar viewing angles or assuming an opacity $\kappa < 2 \text{ cm}^2 \text{ g}^{-1}$. A more stringent limit of $M_{\text{ej}} \lesssim 0.03 M_{\odot}$ can be placed assuming a distance of 215 Mpc. Using the constraints that we obtained for the ejecta mass, we showed how the phase space of the NSBH binary system can also be constrained. In particular, reliable constraints on the highest possible value of the BH spin component aligned with the orbital momentum as a function of Q and Λ_{NS} can be placed for $M_{\text{ej}} < 0.03 M_{\odot}$. For example, assuming a tidal deformability at the high end of the range allowed by GW observations of GW170817, we can constrain the spin component to be $\chi < 0.7$ for mass ratios $Q < 6$. The nondetection of a viable counterpart to S190814bv is also consistent with the progenitor being a low-mass binary BH, rather than an NSBH system.

Follow-up observations of new NSBH mergers with DECam and transient characterization with telescope networks have great potential to unveil EM counterparts during O3 and beyond. Nondetections such as this one can significantly constrain the parameter space of NSBH merger and kilonova models. In the near future, follow-up campaigns with LSST will allow us to probe NSBH mergers deeper and at larger distances.

This work was supported by the GROWTH (Global Relay of Observatories Watching Transients Happen) project funded by the National Science Foundation under PIRE grant No. 1545949. GROWTH is a collaborative project among California Institute of Technology (USA), University of Maryland College Park (USA), University of Wisconsin Milwaukee (USA), Texas Tech University (USA), San Diego State University (USA), University of Washington (USA), Los Alamos National Laboratory (USA), Tokyo Institute of Technology (Japan), National Central University (Taiwan), Indian Institute of Astrophysics (India), Indian Institute of Technology Bombay (India), Weizmann Institute of Science (Israel), The Oskar Klein Centre at Stockholm University (Sweden), Humboldt University (Germany), Liverpool John Moores University (UK), and University of Sydney (Australia).

D.A.G. acknowledges support from Hubble Fellowship grant *HST*-HF2-51408.001-A. Support for program No. *HST*-HF2-51408.001-A is provided by NASA through a grant from the Space Telescope Science Institute, which is operated by the Association of Universities for Research in Astronomy, Inc., under NASA contract NAS5-26555. We gratefully acknowledge Amazon Web Services, Inc., for a generous grant (*PS_IK_FY2019_Q3_Caltech_Gravitational_Wave*) that funded our use of the Amazon Web Services cloud computing infrastructure to process the DECam data. P.E.N. acknowledges support from the DOE through DE-FOA-0001088, Analytical Modeling for Extreme-Scale Computing Environments. D.A.P.

and D.A.G. performed the work associated with this project at the Aspen Center for Physics, which is supported by National Science Foundation grant PHY-1607611. This work was partially supported by a grant from the Simons Foundation. A.J.C.-T. thanks I. Agudo, J. Cepa, V. Dhillon, J. A. Font, A. Martin-Carrillo, S. R. Oates, S. B. Pandey, E. Pian, R. Sanchez-Ramirez, A. M. Sintes, V. Sokolov, and B.-B. Zhang for fruitful conversations. F.F. gratefully acknowledges support from NASA through grant 80NSSC18K0565 and from the NSF through grant PHY1806278. M.B., A.G., E.K., S.D., and J.S. acknowledge support from the G.R.E.A.T research environment funded by the Swedish National Science Foundation. J.S. acknowledges support from the Knut and Alice Wallenberg Foundation. J.S.B. and K.Z. are partially supported by a Gordon and Betty Moore Foundation Data-Driven Discovery grant. D.A.H.B. acknowledges research support from the National Research Foundation of South Africa. M.W.C. is supported by the David and Ellen Lee Postdoctoral Fellowship at the California Institute of Technology. S.N. and G.R. are grateful for support from VIDI, Projectruimte, and TOP Grants of the Innovational Research Incentives Scheme (Vernieuwingsimpuls) financed by the Netherlands Organization for Scientific Research (NWO). H.K. and K.Z. thank the LSSTC Data Science Fellowship Program, which is funded by LSSTC, NSF Cybertraining grant No. 1829740, the Brinson Foundation, and the Moore Foundation; his participation in the program has benefited this work. D.D. is supported by an Australian Government Research Training Program Scholarship. P.G. is supported by NASA Earth and Space Science Fellowship (ASTRO18F-0085). D.L.K. was supported by NSF grant AST-1816492. Y.D.H. thanks the support by the program of China Scholarships Council (CSC) under grant No. 201406660015. A.K.H.K. acknowledges support from the Ministry of Science and Technology of the Republic of China (Taiwan) through grants 107-2628-M-007-003 and 108-2628-M-007-005-RSP. V.Z.G. acknowledges support from the University of Washington College of Arts and Sciences, Department of Astronomy, and the DIRAC Institute. University of Washington's DIRAC Institute is supported through generous gifts from the Charles and Lisa Simonyi Fund for Arts and Sciences and the Washington Research Foundation. M.J. and A.C. acknowledge the support of the Washington Research Foundation Data Science Term Chair fund and the UW Provost's Initiative in Data-Intensive Discovery. S.M. thanks the LSSTC Data Science Fellowship Program, which is funded by LSSTC, NSF Cybertraining Grant-1829740, the Brinson Foundation, and the Moore Foundation; his participation in the program has benefited this work. M.G. is supported by the Polish NCN MAESTRO grant 2014/14/A/ST9/00121.

This research has made use of the VizieR catalog access tool, CDS, Strasbourg, France (doi:10.26093/cds/vizier). The original description of the VizieR service was published in A&AS 143, 23. This project used data obtained with the Dark Energy Camera (DECam), which was constructed by the Dark Energy Survey (DES) collaborating institutions: Argonne National Lab, University of California Santa Cruz, University of Cambridge, Centro de Investigaciones Energeticas, Medioambientales y Tecnologicas-Madrid, University of Chicago, University College London, DES-Brazil consortium, University of Edinburgh, ETH-Zurich, University of Illinois at Urbana-Champaign, Institut de Ciencies de l'Espai, Institut de Fisica d'Altes Energies, Lawrence Berkeley National Lab, Ludwig-Maximilians Universitat, University of Michigan, National Optical Astronomy Observatory, University of Nottingham, Ohio State

University, University of Pennsylvania, University of Portsmouth, SLAC National Lab, Stanford University, University of Sussex, and Texas A&M University. Funding for DES, including DECam, has been provided by the U.S. Department of Energy, National Science Foundation, Ministry of Education and Science (Spain), Science and Technology Facilities Council (UK), Higher Education Funding Council (England), National Center for Supercomputing Applications, Kavli Institute for Cosmological Physics, Financiadora de Estudos e Projetos, Fundação Carlos Chagas Filho de Amparo a Pesquisa, Conselho Nacional de Desenvolvimento Científico e Tecnológico and the Ministério da Ciência e Tecnologia (Brazil), the German Research Foundation-sponsored cluster of excellence “Origin and Structure of the Universe,” and the DES collaborating institutions.

The Liverpool Telescope is operated on the island of La Palma by Liverpool John Moores University in the Spanish Observatorio del Roque de los Muchachos of the Instituto de Astrofísica de Canarias with financial support from the UK Science and Technology Facilities Council. Based on observations made with the Gran Telescopio Canarias (GTC), installed in the Spanish Observatorio del Roque de los Muchachos of the Instituto de Astrofísica de Canarias, in the island of La Palma. This work is partly based on data obtained with the instrument OSIRIS, built by a Consortium led by the Instituto de Astrofísica de Canarias in collaboration with the Instituto de Astronomía of the Universidad Autónoma de México. OSIRIS was funded by GRANTECAN and the National Plan of Astronomy and Astrophysics of the Spanish Government. Some of the observations reported in this paper were obtained with the Southern African Large Telescope (SALT). Polish participation in SALT is funded by grant No. MNiSW DIR/WK/2016/07.

ORCID iDs

Igor Andreoni  <https://orcid.org/0000-0002-8977-1498>
 Daniel A. Goldstein  <https://orcid.org/0000-0003-3461-8661>
 Mansi M. Kasliwal  <https://orcid.org/0000-0002-5619-4938>
 Peter E. Nugent  <https://orcid.org/0000-0002-3389-0586>
 Rongpu Zhou  <https://orcid.org/0000-0001-5381-4372>
 Jeffrey A. Newman  <https://orcid.org/0000-0001-8684-2222>
 Mattia Bulla  <https://orcid.org/0000-0002-8255-5127>
 Kenta Hotokezaka  <https://orcid.org/0000-0002-2502-3730>
 Samaya Nissanke  <https://orcid.org/0000-0001-6573-7773>
 Geert Raaijmakers  <https://orcid.org/0000-0002-9397-786X>
 Jacob E. Jencson  <https://orcid.org/0000-0001-5754-4007>
 Tomás Ahumada  <https://orcid.org/0000-0002-2184-6430>
 Christopher M. Copperwheat  <https://orcid.org/0000-0001-7983-8698>
 Michael W. Coughlin  <https://orcid.org/0000-0002-8262-2924>
 S. Bradley Cenko  <https://orcid.org/0000-0003-1673-970X>
 Daniel A. Perley  <https://orcid.org/0000-0001-8472-1996>
 David O. Cook  <https://orcid.org/0000-0002-6877-7655>
 Jeff Cooke  <https://orcid.org/0000-0001-5703-2108>
 Suhail Dhawan  <https://orcid.org/0000-0002-2376-6979>
 Dougal Dobie  <https://orcid.org/0000-0003-0699-7019>
 Pradip Gatkine  <https://orcid.org/0000-0002-1955-2230>
 V. Zach Golkhou  <https://orcid.org/0000-0001-8205-2506>
 Ariel Goobar  <https://orcid.org/0000-0002-4163-4996>
 Andreas Guerra Chaves  <https://orcid.org/0000-0001-9560-2220>

Matthew Hankins  <https://orcid.org/0000-0001-9315-8437>
 David L. Kaplan  <https://orcid.org/0000-0001-6295-2881>
 Albert K. H. Kong  <https://orcid.org/0000-0002-5105-344X>
 Erik C. Kool  <https://orcid.org/0000-0002-7252-3877>
 Jesper Sollerman  <https://orcid.org/0000-0003-1546-6615>
 Anastasios Tzanidakis  <https://orcid.org/0000-0003-0484-3331>
 Sara Webb  <https://orcid.org/0000-0003-2601-1472>
 Keming Zhang  <https://orcid.org/0000-0002-9870-5695>

References

- Abadie, J., Abbott, B. P., Abbott, R., et al. 2010, *CQGrA*, 27, 173001
 Abbott, B. P., Abbott, R., Abbott, T. D., et al. 2016, *PhRvL*, 116, 061102
 Abbott, B. P., Abbott, R., Abbott, T. D., et al. 2017, *PhRvL*, 119, 161101
 Abbott, B. P., Abbott, R., Abbott, T. D., et al. 2019, *PhRvX*, 9, 031040
 Andreoni, I., Goldstein, D. A., Ahumada, T., et al. 2019, GCN, 25362
 Annis, J., Herner, K., & Soares-Santos, M. 2019, GCN, 25458
 Barbieri, C., Salafia, O. S., Perego, A., Colpi, M., & Ghirlanda, G. 2019, *A&A*, 625, A152
 Becker, A. 2019, HOTPANTS: High Order Transform of PSF ANd Template Subtraction (v 5.1.10b), Astrophysics Source Code Library, ascl:1504.004
 Belkin, S., Pozanenko, A., Inasaridze, R. Y., et al. 2019, GCN, 25392
 Blagorodnova, N., Neill, J. D., Walters, R., et al. 2018, *PASP*, 130, 035003
 Blondin, S., & Tonry, J. L. 2007, *ApJ*, 666, 1024
 Bruun, S. H., Sagues Carracedo, A., Chen, T. W., et al. 2019, GCN, 25384
 Buckley, D., Ciroi, S., Gromadzki, M., et al. 2019, GCN, 25481
 Buckley, D. A. H., Andreoni, I., Barway, S., et al. 2018, *MNRAS*, 474, L71
 Buckley, D. A. H., Swart, G. P., & Meiring, J. G. 2006, *Proc. SPIE*, 6267, 62670Z
 Bulla, M. 2019, *MNRAS*, 489, 5037
 Bulla, M., Covino, S., Kyutoku, K., et al. 2019, *NatAs*, 3, 99
 Burgh, E. B., Nordsteck, K. H., Kobulnicky, H. A., et al. 2003, *Proc. SPIE*, 4841, 1463
 Burrows, D. N., Hill, J. E., Nousek, J. A., et al. 2005, *SSRv*, 120, 165
 Castro-Tirado, A. J., Valeev, A. F., Hu, Y. D., et al. 2019, GCN, 25543
 Cepa, J., Aguiar, M., Escalera, V. G., et al. 2000, *Proc. SPIE*, 4008, 623
 Chambers, K. C., Magnier, E. A., Metcalfe, N., et al. 2016, arXiv:1612.05560
 Chen, T. W., Schweyer, T., Nicuesa Guelbenzu, A., et al. 2019, GCN, 25457
 Christie, I. M., Lalakos, A., Tchekhovskoy, A., et al. 2019, *MNRAS*, 490, 4811
 Colless, M., Dalton, G., Maddox, S., et al. 2001, *MNRAS*, 328, 1039
 Corre, D., Blazek, M., Klotz, A., et al. 2019, GCN, 25599
 Corwin, H. G., Jr., Buta, R. J., & de Vaucouleurs, G. 1994, *AJ*, 108, 2128
 Coughlin, M., Ahumada, T., & Anand, S. 2019a, GCN, 25477
 Coughlin, M. W., Dietrich, T., Antier, S., et al. 2019b, *MNRAS*, 492, 863
 Coughlin, M. W., Dietrich, T., Margalit, B., & Metzger, B. D. 2019c, *MNRAS*, 489, L91
 Coulter, D. A., Foley, R. J., Kilpatrick, C. D., et al. 2017, *Sci*, 358, 1556
 Cowperthwaite, P. S., Berger, E., Villar, V. A., et al. 2017, *ApJL*, 848, L17
 Crawford, S. M., Still, M., Schellart, P., et al. 2010, *Proc. SPIE*, 7737, 773725
 Cushing, M. C., Vacca, W. D., & Rayner, J. T. 2004, *PASP*, 116, 362
 Dályá, G., Galgóczi, G., Dobos, L., et al. 2018, *MNRAS*, 479, 2374
 Dark Energy Survey Collaboration, Abbott, T., Abdalla, F. B., et al. 2016, *MNRAS*, 460, 1270
 D’Avanzo, P., Giunta, A., Izzo, L., et al. 2019, GCN, 25401
 De, K., Goldstein, D., Andreoni, I., et al. 2019a, GCN, 25348
 De, K., Jencson, J., Kasliwal, M. M., Goldstein, D., & Andreoni, I. 2019b, GCN, 25478
 De, K., Kasliwal, M. M., Andreoni, I., Karambelkar, V., & Sharma, Y. 2019c, GCN, 25461
 De, K., Tinyantont, S., Kamraj, N., et al. 2019d, GCN, 25396
 de Vaucouleurs, G., de Vaucouleurs, A., Corwin, H. G., Jr., et al. 1991, Third Reference Catalogue of Bright Galaxies. Volume I: Explanations and References. Volume II: Data for Galaxies between 0^h and 12^h. Volume III: Data for Galaxies between 12^h and 24^h (New York: Springer)
 Dey, A., Schlegel, D. J., Lang, D., et al. 2019, *AJ*, 157, 168
 Dhawan, S., Bulla, M., Goobar, A., Sagués Carracedo, A., & Setzer, C. N. 2020, *ApJ*, 888, 67
 Dichiarà, S., Troja, E., Cenko, S. B., et al. 2019a, GCN, 25374
 Dichiarà, S., Troja, E., Cenko, S. B., et al. 2019b, GCN, 25397
 Dichiarà, S., Troja, E., Watson, A. M., et al. 2019c, GCN, 25416
 Dobie, D., Murphy, T., Lenc, E., et al. 2019, GCN, 25472
 Drout, M. R., Piro, A. L., Shappee, B. J., et al. 2017, *Sci*, 358, 1570

- Evans, P. A., Kennea, J. A., Tohuvaovohu, A., et al. 2019, GCN, 25400
- Fernández, R., Foucart, F., Kasen, D., et al. 2017, *CQGra*, **34**, 154001
- Fernández, R., Kasen, D., Metzger, B. D., & Quataert, E. 2015, *MNRAS*, **446**, 750
- Fernandez, R., & Metzger, B. D. 2013, *MNRAS*, **435**, 502
- Fernández, R., & Metzger, B. D. 2016, *ARNPS*, **66**, 23
- Fernández, R., Tchekhovskoy, A., Quataert, E., Foucart, F., & Kasen, D. 2019, *MNRAS*, **482**, 3373
- Flanagan, É É, & Hinderer, T. 2008, *PhRvD*, **77**, 021502
- Flaugher, B., Diehl, H. T., Honscheid, K., et al. 2015, *AJ*, **150**, 150
- Foucart, F. 2012, *PhRvD*, **86**, 124007
- Foucart, F., Hinderer, T., & Nissanke, S. 2018, *PhRvD*, **98**, 081501
- Fremling, C., Goldstein, D., Andreoni, I., & Kasliwal, M. M. 2019, GCN, 25460
- Fremling, C., Sollerman, J., Taddia, F., et al. 2016, *A&A*, **593**, A68
- Geesaman, D. 2015, APS Meeting, *AA1.001*
- Gehrels, N., Cannizzo, J. K., Kanner, J., et al. 2016, *ApJ*, **820**, 136
- Goldstein, D. A., & Anand, S. 2019, GCN, 25393
- Goldstein, D. A., Andreoni, I., Hankins, M., et al. 2019a, GCN, 25393
- Goldstein, D. A., Andreoni, I., Nugent, P. E., et al. 2019b, *ApJL*, **881**, L7
- Goldstein, D. A., Andreoni, I., Zhou, R., et al. 2019c, GCN, 25391
- Goldstein, D. A., D'Andrea, C. B., Fischer, J. A., et al. 2015, *AJ*, **150**, 82
- Goldstein, D. A., Perley, D., Andreoni, I., & Kasliwal, M. M. 2019d, GCN, 25355
- Gomez, S., Hosseinzadeh, G., Berger, E., et al. 2019, GCN, 25483
- Gomez, S., Hosseinzadeh, G., Cowperthwaite, P. S., et al. 2019, *ApJL*, **884**, L55
- Greggio, L., Rejkuba, M., Gonzalez, O. A., et al. 2014, *A&A*, **562**, A73
- Herner, K., Palmese, A., Soares-Santos, M., et al. 2019a, GCN, 25373
- Herner, K., Palmese, A., Soares-Santos, M., et al. 2019b, GCN, 25398
- Hinderer, T., Lackey, B. D., Lang, R. N., & Read, J. S. 2010, *PhRvD*, **81**, 123016
- Hotokezaka, K., & Nakar, E. 2019, arXiv:1909.02581
- Hu, Y. D., Castro-Tirado, A. J., Valeev, A. F., et al. 2019, GCN, 25588
- Huber, M., Smith, K. W., Chambers, K., et al. 2019, GCN, 25356
- Jonker, P., Maguire, K., Fraser, M., et al. 2019, GCN, 25454
- Kasen, D., Metzger, B., Barnes, J., Quataert, E., & Ramirez-Ruiz, E. 2017, *Natur*, **551**, 80
- Kasliwal, M. M., Cannella, C., Bagdasaryan, A., et al. 2019, *PASP*, **131**, 038003
- Kasliwal, M. M., Nakar, E., Singer, L. P., et al. 2017, *Sci*, **358**, 1559
- Kawaguchi, K., Kyutoku, K., Nakano, H., et al. 2015, *PhRvD*, **92**, 024014
- Kawaguchi, K., Kyutoku, K., Shibata, M., & Tanaka, M. 2016, *ApJ*, **825**, 52
- Kilpatrick, C. D., Foley, R. J., Kasen, D., et al. 2017, *Sci*, **358**, 1583
- Kobulnicky, H. A., Nordsieck, K. H., Burgh, E. B., et al. 2003, *Proc. SPIE*, **4841**, 1634
- Lattimer, J. M., & Schramm, D. N. 1974, *ApJL*, **192**, L145
- LIGO Scientific Collaboration & Virgo Collaboration 2019, GCN, 24448
- Lipunov, V., Vlasenko, D., Gorbvskoy, E., et al. 2019, GCN, 25474
- Lopez-Cruz, O., Castro-Tirado, A. J., Macri, L., et al. 2019a, GCN, 25571
- Lopez-Cruz, O., Castro-Tirado, A. J., Macri, L., et al. 2019b, GCN, 25419
- Luri, X., Brown, A. G. A., Sarro, L. M., et al. 2018, *A&A*, **616**, A9
- McBrien, O. R., Srivastav, S., Smith, K. W., et al. 2019, GCN, 25346
- Metzger, B. D., & Berger, E. 2012, *ApJ*, **746**, 48
- Miller, J. M., Ryan, B. R., Dolence, J. C., et al. 2019, *PhRvD*, **100**, 023008
- Mingarelli, C. M. F., Levin, J., & Lazio, T. J. W. 2015, *ApJL*, **814**, L20
- Mooley, K., Hallinan, G., Kasliwal, M. M., Corsi, A., & Frail, D. 2019, GCN, 25480
- Nakar, E. 2019, arXiv:1912.05659
- Nissanke, S., Kasliwal, M., & Georgieva, A. 2013, *ApJ*, **767**, 124
- Nordin, J., Brinnel, V., & Giomi, M. 2019, Transient Name Server Discovery Report, 2019-1370, 1
- Oke, J. B., Cohen, J. G., Carr, M., et al. 1995, *PASP*, **107**, 375
- Özel, F., & Freire, P. 2016, *ARA&A*, **54**, 401
- Palmese, A., Annis, J., & Soares-Santos, M. 2019, GCN, 25468
- Perley, D. A. 2019, *PASP*, **131**, 084503
- Planck Collaboration, Ade, P. A. R., Aghanim, N., et al. 2016, *A&A*, **594**, A13
- Rodríguez, O., Meza-Retamal, N., Quirola, J., et al. 2019, GCN, 25423
- Schutz, B. F. 1986, *Natur*, **323**, 310
- Siegel, D. M., & Metzger, B. D. 2017, *PhRvL*, **119**, 231102
- Siegel, D. M., & Metzger, B. D. 2018, *ApJ*, **858**, 52
- Singer, L. P., Chen, H.-Y., Holz, D. E., et al. 2016, *ApJL*, **829**, L15
- Smartt, S., Smith, K. W., Srivastav, S., et al. 2019, GCN, 25455
- Soares-Santos, M., Annis, J., Garcia, A., et al. 2019a, GCN, 25425
- Soares-Santos, M., Annis, J., Garcia, A., et al. 2019b, GCN, 25438
- Soares-Santos, M., Annis, J., Herner, K., et al. 2019c, GCN, 25486
- Soares-Santos, M., Tucker, D., Allam, S., et al. 2019d, GCN, 25336
- Steele, I. A., Smith, R. J., Rees, P. C., et al. 2004, *Proc. SPIE*, **5489**, 679
- Tanaka, M., Kato, D., Gaigalas, G., et al. 2018, *ApJ*, **852**, 109
- The LIGO Scientific Collaboration & the Virgo Collaboration 2019a, GCN, 24228, 1
- The LIGO Scientific Collaboration & the Virgo Collaboration 2019b, GCN, 25324
- The LIGO Scientific Collaboration & the Virgo Collaboration 2019c, GCN, 24277, 1
- The LIGO Scientific Collaboration & the Virgo Collaboration 2019d, GCN, 25333
- Tucker, D., Allam, S., Wiesner, M., et al. 2019a, GCN, 25379
- Tucker, D., Butner, M., Wiesner, M., et al. 2019b, GCN, 25484
- Veitch, J., Raymond, V., Farr, B., et al. 2015, *PhRvD*, **91**, 042003
- Wang, X., Antier, S., Coughlin, M., et al. 2019, GCN, 25485
- Wiesner, M., Butner, M., Allam, S., et al. 2019a, GCN, 25596
- Wiesner, M., Butner, M., Tucker, D., et al. 2019b, GCN, 25540
- Wilson, J. C., Eikenberry, S. S., Henderson, C. P., et al. 2003, *Proc. SPIE*, **4841**, 451
- Wright, E. L., Eisenhardt, P. R. M., Mainzer, A. K., et al. 2010, *AJ*, **140**, 1868
- Yang, S., Cappellaro, E., Grado, A., et al. 2019, GCN, 25748